



HAL
open science

Characterization of pore structure and strain localization in Majella limestone by X-ray computed tomography and digital image correlation

Yuntao Ji, Hall Stephen A., Patrick Baud, Teng-Fong Wong

► **To cite this version:**

Yuntao Ji, Hall Stephen A., Patrick Baud, Teng-Fong Wong. Characterization of pore structure and strain localization in Majella limestone by X-ray computed tomography and digital image correlation. *Geophysical Journal International*, 2015, pp.700-719. 10.1093/gji/ggu414 . hal-01141102

HAL Id: hal-01141102

<https://hal.science/hal-01141102>

Submitted on 8 Nov 2021

HAL is a multi-disciplinary open access archive for the deposit and dissemination of scientific research documents, whether they are published or not. The documents may come from teaching and research institutions in France or abroad, or from public or private research centers.

L'archive ouverte pluridisciplinaire **HAL**, est destinée au dépôt et à la diffusion de documents scientifiques de niveau recherche, publiés ou non, émanant des établissements d'enseignement et de recherche français ou étrangers, des laboratoires publics ou privés.



Distributed under a Creative Commons Attribution 4.0 International License

Characterization of pore structure and strain localization in Majella limestone by X-ray computed tomography and digital image correlation

Yuntao Ji,¹ Stephen A. Hall,² Patrick Baud³ and Teng-fong Wong^{4,5}

¹State Key Laboratory of Earthquake Dynamics, Institute of Geology, China Earthquake Administration, Beijing 100029, China

²Division of Solid Mechanics, Lund University, Lund Sweden and European, Spallation Source AB, Lund, Sweden

³Institut de Physique du Globe de Strasbourg (UMR 7516 CNRS, Université de Strasbourg/EOST), Strasbourg, France. E-mail: patrick.baud@unistra.fr

⁴Department of Geosciences, Stony Brook University, NY 11790-2100, USA

⁵Earth System Science Programme, Faculty of Science, The Chinese University of Hong Kong, Hong Kong

Accepted 2014 October 20. Received 2014 October 12; in original form 2014 February 24

SUMMARY

Standard techniques for computed tomography imaging are not directly applicable to a carbonate rock because of the geometric complexity of its pore space. In this study, we first characterized the pore structure in Majella limestone with 30 per cent porosity. Microtomography data acquired on this rock was partitioned into three distinct domains: macropores, solid grains, and an intermediate domain made up of voxels of solid embedded with micropores below the resolution. A morphological analysis of the microtomography images shows that in Majella limestone both the solid and intermediate domains are interconnected in a manner similar to that reported previously in a less porous limestone. We however show that the macroporosity in Majella limestone is fundamentally different, in that it has a percolative backbone which may contribute significantly to its permeability. We then applied for the first time 3-D-volumetric digital image correlation (DIC) to characterize the mode of mechanical failure in this limestone. Samples were triaxially deformed over a wide range of confining pressures. Tomography imaging was performed on these samples before and after deformation. Inelastic compaction was observed at all tested pressures associated with both brittle and ductile behaviors. Our DIC analysis reveals the structure of compacting shear bands in Majella limestone deformed in the transitional regime. It also indicates an increase of geometric complexity with increasing confinement—from a planar shear band, to a curvilinear band, and ultimately to a diffuse multiplicity of bands, before shear localization is inhibited as the failure mode completes the transition to delocalized cataclastic flow.

Key words: Microstructures; Permeability and porosity; Creep and deformation; Elasticity and anelasticity.

1 INTRODUCTION

The transition of failure mode in porous rock from brittle faulting to distributed cataclastic flow is a topic of importance in many geological applications, including the mechanics of faulting and deformation band formation (Aydin & Johnson 1978; Shipton & Cowie 2001; Aydin *et al.* 2006), tectonic evolution and fluid flow in sedimentary formations (Antonellini *et al.* 1994; Casey & Butler 2004; Eichhubl *et al.* 2004, 2010; Sheldon *et al.* 2006), as well as reservoir compaction and subsidence (Boutéca *et al.* 1996; Fisher *et al.* 1999). Recent advances in rock mechanics research in this area was reviewed by Wong & Baud (2012), who emphasized the importance of integrating data on mechanical deformation and failure mode with systematic microstructural observations of both the

pre-existing pore structure and damage development to gain insights into the operative mechanisms.

Traditionally, pore space in rock is characterized using optical and scanning electron microscopes (SEM). Supplementary information on geometry of the pores and throats may also be gained from mercury injection (Churcher *et al.* 1991) and nuclear magnetic resonance (NMR) imaging (Gleeson & Woessner 1991; Kleinberg 1999). Furthermore, advances in 3-D imaging techniques such as X-ray computed tomography (CT) and laser scanning confocal microscopy (Fredrich *et al.* 1995) have furnished enhanced perspective on pore geometry complexity. In particular, X-ray CT has been used widely for characterizing porous clastic rocks such as sandstone, whose void space is dominated by relatively equant pores connected by throats that are sufficiently large for direct imaging

by X-ray micro-CT. Such data have elucidated the 3-D geometric complexity (Lindquist *et al.* 2000) and its control over elastic and transport properties (Arns *et al.* 2004; Fredrich *et al.* 2006; Knackstedt *et al.* 2009; Zhan *et al.* 2010; Sun *et al.* 2011) of naturally and experimentally deformed sandstones.

When images of a rock sample are acquired before and after deformation in rock mechanics experiments, digital image correlation (DIC) can be used to infer the displacement and strain fields. This correlation technique has been used widely in experimental mechanics to map out the spatial distribution of deformation based on photographs of the surface of deforming specimens, and more recently on X-ray CT images in 3-D. It can effectively delineate the nucleation and development of damage in synthetic (Russell & Sutton 1989; Bastawros *et al.* 2000; Wattrisse *et al.* 2001) and biomedical (Bay *et al.* 1999; Wang *et al.* 2002) materials, as well as in geomaterials such as sand and sandstone (Rechenmacher & Finno 2004; Lenoir *et al.* 2007; Louis *et al.* 2007; Hall *et al.* 2010; Charalampidou *et al.* 2011).

These 3-D imaging techniques have not been widely employed for carbonate rocks, even though this sedimentary rock type hosts more than half of the world's oil reserves and is, in this regard, as important as clastic rocks. The limited use on carbonates arises primarily because their pore geometry is significantly more complex than that of sandstones (Choquette & Pray 1970; Lucia 1995), and consequently micro-CT cannot directly image certain fine details of the pore space (Okabe & Blunt 2007; Bauer *et al.* 2011; Ji *et al.* 2012). Complexity of carbonate pore geometry arises from depositional environment and diagenesis, which exert significant influence over the development of their texture and fabric (Folk 1980), and in turn significantly modify both the size and connectivity of the pore space. Accordingly the pore size in a carbonate rock may span over a very broad range, often with a bimodal distribution which comprises macroporosity and a significant fraction of microporosity with submicron features not readily resolved by micro-CT (Pittman 1971; Anselmetti *et al.* 1998).

Recent rock physics studies have demonstrated that the macropores and micropores exert distinct influences on the elastic (Baechle *et al.* 2008; Knackstedt *et al.* 2009) and inelastic (Zhu *et al.* 2010; Vajdova *et al.* 2012) behaviors of limestone. Even though most micropores can be resolved under the SEM, quantitative characterization of a statistically representative ensemble of these fine features can be tedious, whereas the 3-D characteristics can only be inferred indirectly from multiple 2-D sections of the sample. In a recent study, Ji *et al.* (2012) developed a more efficient methodology based on X-ray micro-CT, and applied it to Indiana limestone. A first objective of this current study is to extend this approach to the Majella limestone with a porosity almost twice that of Indiana limestone. Statistics of the macropore size and the spatial distribution of microporosity in 3-D were characterized. These data provide useful insights into the complexity of the pore geometry and its connectivity, as well as their potential influence on mechanical and hydraulic behaviour. This provides the context for the second objective of this study, which was to investigate the mode of mechanical failure using 3-D volumetric DIC.

The failure mode transition in Majella limestone was recently studied by Baud *et al.* (2009) and Vajdova *et al.* (2012). In the brittle faulting regime, failure in such a porous limestone develops by shear localization and the strength is sensitively dependent on the porosity. Under high confinement, failure develops by distributed cataclastic flow, and the compactive yield stress is dependent on not only the total porosity, but also the micropore size, as well as the partitioning between microporosity and macroporosity (Zhu *et al.*

2010). Optical and SEM observations have documented the micromechanical processes and damage evolution associated with the brittle and ductile end-members, which include pore-emanated microcracking and cataclastic pore collapse, respectively (Baud *et al.* 2009; Vajdova *et al.* 2012).

However, regarding the failure mode and damage development in the transitional regime from brittle faulting to cataclastic flow, these recent studies were inconclusive. One might surmise that strain localization features such as high-angle shear bands would develop in a porous limestone, analogous to failure modes observed in the transitional regime in porous sandstone (Bésuelle *et al.* 2003; Baud *et al.* 2004). However, such microstructural development is not evident in thin-sections of failed limestone samples in the transitional regime, and therefore several questions remain unanswered. Is strain localization absent, or the clustering of damage too subtle to be resolved by optical and SEM observations? If indeed failure in the transitional regime involves strain localization, how early in the deformation history would it initiate? What are the micromechanical processes, and how is the damage partitioned between the macroporosity and microporosity? Another objective of this study is to resolve these questions using DIC in conjunction with microstructural observations and CT imaging of samples before and after failure. This approach would allow one to identify with relatively high resolution the onset of strain localization and to infer the failure mode.

To tackle this second objective, four Majella limestone samples were triaxially compressed at confining pressures ranging from 5 to 25 MPa and another under hydrostatic conditions up to 60 MPa. For each of these five samples, two CT images were acquired before and after the deformation. We then used the TomoWarp code (Hall *et al.* 2009) to perform 3-D volumetric DIC on the pairs of images to derive the permanent displacement field and the full 3-D strain tensor field of each sample. This code has proven to be very effective for mapping out 3-D complexity of strain localization in porous sandstone (Charalampidou *et al.* 2011, 2014), and our study constitutes its first application to a limestone.

2 EXPERIMENTAL PROCEDURE

Our samples are from the Madonna delle Mazze quarry in the Apennines, Central Italy, located on the inner part of the forelimb of the Majella anticline, where fault development related to deformation bands and stylolites has been investigated by Tondi *et al.* (2006); Ciona *et al.* (2012) and Rustichelli *et al.* (2012). Our samples are from two different blocks of Majella limestone acquired from the relatively undeformed host rock. The sample for micro-CT analysis was from the block used by Baud *et al.* (2009), who have conducted comprehensive deformation experiments in relation to the brittle–ductile transition. Recently, Vajdova *et al.* (2012) have used optical and SEM to conduct a detailed characterization of the pore geometry of an undeformed sample as well as damage in deformed samples from an identical block. We will refer to samples from this block as Majella1. For mechanical deformation in this study, we used samples cored from a different block from the same locality, which will be denoted as Majella2.

2.1 Sample preparation and mechanical deformation

Cylindrical samples of Majella2 were cored perpendicular to the sedimentary bedding and then ground to diameter of 20 mm and length of 40 mm. Jacketed samples were deformed in conventional

Table 1. Deformation history of samples studied.

Confining pressure (MPa)	Initial porosity (per cent)	Axial strain (per cent)	Analysis	Comments
60	32.4	–	DIC	Hydrostat beyond P*: cataclastic flow
5	32.7	0.91	DIC	High angle compacting shear bands
10	32.9	1	DIC	High angle compacting shear bands
15	32.6	1.46	DIC	Multiple strands of closely spaced tortuous bands
25	32.3	1.56	DIC	Multiple strands of closely spaced tortuous bands

triaxial configuration at room temperature at Ecole et Observatoire des Sciences de la Terre in Strasbourg, France, following the protocol of Baud *et al.* (2009). Axial displacement was measured outside the pressure vessel with a capacitive transducer (with accuracy 0.2 μm) mounted on the moving piston and servo-controlled at a fixed rate (corresponding to a nominal strain rate of $10^{-5}/\text{s}$). Axial strain of a sample was calculated from the axial displacement data and initial sample length, accounting for stiffness of the loading frame. Volumetric strain was inferred from the displacement of the piston of the confining pressure generator measured with an angular encoder.

To study the brittle–ductile transition and strain localization, we triaxially deformed four samples at confining pressures of 5, 10, 15 and 25 MPa, respectively. Another sample was hydrostatically compressed to a maximum pressure of 60 MPa. The five Majella2 samples and their deformation histories are summarized in Table 1.

2.2 X-ray micro-CT and microstructural analysis

For each of the five samples of Majella 2, CT data were acquired at the X-ray scanning facility of Laboratoire 3SR laboratory in Grenoble, France, before and after the deformation, following the procedure described by Charalampidou *et al.* (2014). These two images were then used for DIC analysis. After retrieval from the apparatus and acquisition of the CT image, the deformed samples were encapsulated with epoxy and two thin sections were then cut along the central vertical plane of each sample. One thin section was used primarily for optical microscopy, and the other was coated with gold for SEM observations. For SEM observations at Stony Brook University, the gold-coated thin sections were studied using a LEO 1550 microscope with a voltage up to 10 kV. All SEM micrographs presented here were acquired in the backscattered electron mode. Optical microscopy was performed using a Nikon polarizing microscope.

The Grenoble X-ray scanning facility employed a 150 kV micro-focal X-ray source capable of a $<5 \mu\text{m}$ focal spot size. X-rays were set to energy of 100 kV and intensity of 100 μA . About 1200 views were gathered, and reconstructed slice images were of size about 1600×1600 voxels. Each sample spanned 1600 image slices, and the voxel size was about $25 \times 25 \times 25 \mu\text{m}^3$.

For micro-CT imaging a subvolume was obtained from an undeformed sample of Majella1 limestone. As described by Ji *et al.* (2012), the cylindrical subvolume (of diameter 4 mm and length 7 mm) was extracted from one half of the sample by coring perpendicular to the cut surface. The imaging of this sample was performed at the High-Resolution CT Facility at the University of Texas at Austin (UTCT), following procedures detailed by Ketcham & Carlson (2001). The system employs a 200 kV microfocal X-ray source capable of a $<10 \mu\text{m}$ focal spot size. X-rays were set to 60 kV and 10 W without any filter, and a $4\times$ objective was employed. Acquisition times ranged from 50 to 60 s per view, and from 476 to 481 views were gathered over an angular range from 190° to 192° . Reconstructed slice images were of size about 1000×1000

voxels. Each sample spanned 934 image slices, and the voxel size was $4 \times 4 \times 4 \mu\text{m}^3$.

2.3 Segmentation and morphological analysis of micro-CT image

We used an approach analogous to that of Ji *et al.* (2012) to segment the micro-CT image into three distinct domains: solid grains, voids with dimensions larger than the voxel resolution, and a zone of intermediate density. We will refer to the voids in the second domain with dimensions larger than the voxel size as ‘macropores’. In the third domain, since the voxel density is lower than grain density, we interpret each voxel to be embedded with numerous voids of subvoxel dimension. These voids will be referred to as ‘micropores’.

In the histogram of the X-ray attenuation coefficient for the 16-bit CT image (Fig. 1a), one can identify a distinct peak (at a grey level of $\sim 3.5 \times 10^4$) corresponding to the solid domain. The distribution is skewed, and to the left of the peak there is an inflection point (at grey level of $\sim 3.4 \times 10^4$). To accentuate the contrast among the solid, void and intermediate zone, it was necessary to apply appropriate filtering before we could segment the image into three phases. Indeed, Bauer *et al.* (2011) also concluded that such pre-segmentation filtering was necessary in their recent study of Estailades and Lavoux limestones (with comparable porosities of 24.7 and 28.7 per cent, respectively).

Based on a comparison of the filtered images with microstructural observations, we concluded that a median filter applied to a volume 5^3 voxels (analogous to that applied by Bauer *et al.* (2011) to their two limestones) provides the optimal resolution of the three domains. Such filtering typically eliminates numerous isolated, relatively small blobs (especially in the intermediate domain), which likely correspond to random noise. Most importantly, a second peak (at a grey level of $\sim 1.6 \times 10^4$) interpreted to correspond to the void domain emerged in the histogram of the filtered image (Fig. 1b).

To segment the CT image into three domains, we followed Ji *et al.* (2012) to select two thresholds I_{void}^* and I_{solid}^* (with $I_{\text{solid}}^* > I_{\text{void}}^*$), located in the region between the two peaks. The two thresholds thus segment the histogram into three domains. The following criterion on the grey level I of a voxel was adopted for identifying to which of the three domains it belongs:

$$\text{Void: } I \leq I_{\text{void}}^* \quad (1a)$$

$$\text{Solid: } I \geq I_{\text{solid}}^* \quad (1b)$$

$$\text{Intermediate: } I_{\text{void}}^* < I < I_{\text{solid}}^* \quad (1c)$$

Whereas local porosity of a voxel in the void and solid domains has values of 0 and 1, respectively, local voxel porosity in the intermediate domain falls between 0 and 1. Since Majella limestone is basically monominerallic (with a modal composition of 99 per cent calcite), the density of the grains is basically homogeneous and density of the porous rock decreases linearly with porosity. Since

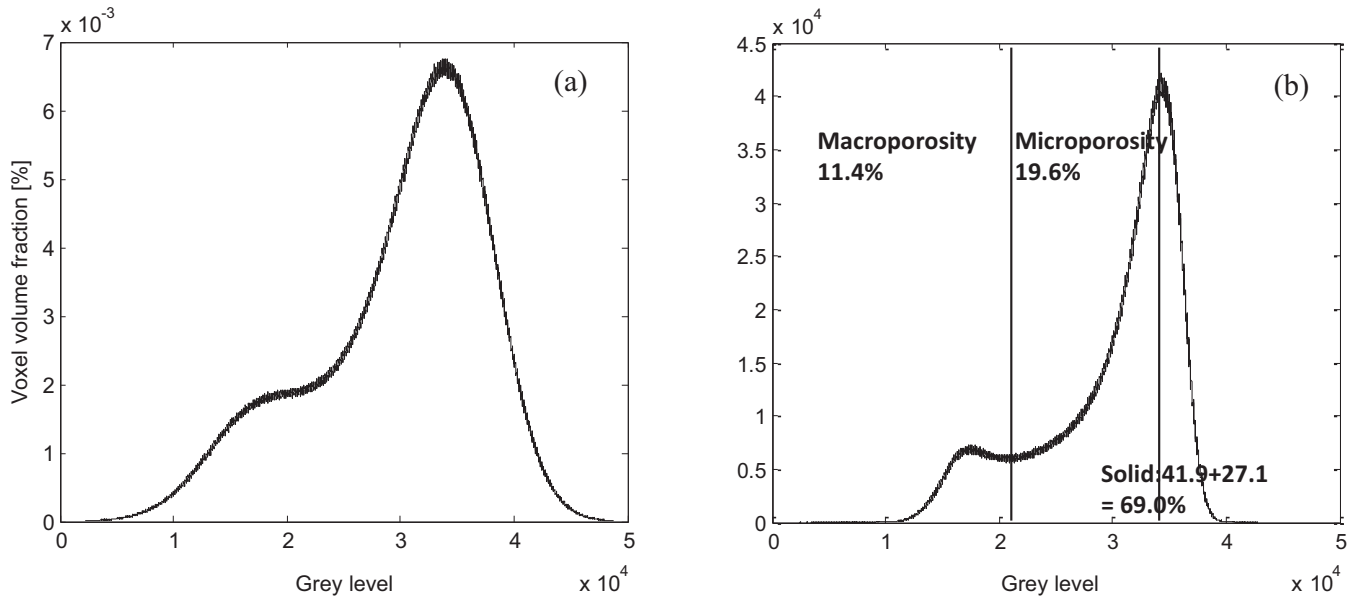


Figure 1. CT data on intact Majella limestone. (a) Distribution of X-ray attenuation (relative frequency) for 16-bit CT image. (b) (left-hand side) Global filtered histogram. The images were segmented with multiple thresholds into three separate domains: solid grains, macroporosity and an intermediate zone dominated by microporosity.

the CT attenuation coefficient is primarily dependent on the density, the grey level of a voxel is also expected to be linearly related to its local porosity ϕ . Accordingly, we adopted the following relation for inferring the local porosity from the CT measurement:

$$\phi = \frac{I_{\text{solid}}^* - I}{I_{\text{solid}}^* - I_{\text{void}}^*}. \quad (2)$$

With the local porosity so defined, we developed a criterion for identifying the two thresholds, for given values of macroporosity Φ_M and microporosity Φ_m . The voxel volume fraction (i.e. voxel volume normalized to the sample volume) at a grey level I is denoted by $f(I)$. Accordingly the macroporosity and microporosity can be obtained by integrating under the histogram as:

$$\Phi_m = \int_{I_{\text{void}}^*}^{I_{\text{solid}}^*} \phi f(I) dI, \quad (3a)$$

$$\Phi_M = \int_0^{I_{\text{void}}^*} f(I) dI. \quad (3b)$$

As noted later, 2-D microstructural measurements indicate that Majella1 has macroporosity and microporosity values of 11.4 and 19.6 per cent, respectively. Imposing these constraints on our micro-CT data (with a median filter applied to 5^3 voxel volume), we determined the threshold grey levels to be $I_{\text{void}}^* = 20\,361$ and $I_{\text{solid}}^* = 34\,250$. Interestingly the thresholds so determined are not very sensitive to filtering. For example, if the median filter were applied to larger voxel volume of 9^3 , the thresholds would be 22 024 and 33 821 instead.

Morphological processing was next performed on the micro-CT image, so as to identify individual clusters of interconnected voxels that correspond to blobs of solid, macroporosity or microporosity. We used a ‘marching cubes’ algorithm (Lorenson & Cline 1987; Ji *et al.* 2012) to map out the surfaces of these blobs. For an isolated macropore with volume V and surface area S , two parameters were used to characterize its geometry:

$$D = \left(\frac{6V}{\pi} \right)^{1/3}, \quad (4a)$$

and

$$\psi = \frac{6V}{DS} = \frac{\pi^{1/3}(6V)^{2/3}}{S}. \quad (4b)$$

The equivalent diameter D is the diameter of a sphere with volume V identical to that of the macropore. The sphericity ψ (Wadell 1935) is the ratio of the surface area of a sphere (with the same volume as the macropore) to the surface area S of the macropore. It is a measure of roundness, such that $\psi = 1$ for a sphere and a ψ value significantly less than unity is associated with a highly non-spherical geometry or relatively rough surface.

2.4 Imaging strain localization

For porous sandstone two techniques have been developed to enhance the contrast and resolve the structural evolution of compacting shear bands and compaction bands. The first technique hinges on the hypothesis that grain crushing in a clastic material would homogenize the spatial distribution of X-ray attenuation (Otani *et al.* 2005), and accordingly the relative dispersion (inferred from of the grey-level statistics in an elemental volume made up of multiple voxels) provides a proxy for the local damage intensity, such that strain localization related to compactant cataclasis would correspond to a zone of relatively low dispersion. This technique has been successfully applied to delineate compacting shear bands and compaction bands in porous sandstones (Louis *et al.* 2006; Charalampidou *et al.* 2011, 2014). However, it is not effective for characterizing localized compaction in a limestone, since the micromechanical processes in this case are fundamentally different from the pervasive grain crushing and comminution in a clastic rock (Zhu *et al.* 2010).

The second technique is DIC, which can map out the spatial distribution of deformation without any assumptions on the operative micromechanical processes or initial homogeneity (Louis *et al.* 2007). Two digital images corresponding to the undeformed and deformed states are compared. Maximizing an appropriate coherency measure (such as the semblance and cross-correlation function) of the spatial distributions of grey level in the two images, the

correspondence between undeformed and deformed coordinates of the same material points in the sample are identified (Bruck *et al.* 1989; Sutton *et al.* 2000). Accordingly the undeformed coordinates can be mapped to the deformed coordinates, which then allows the displacement and strain fields to be inferred. Using the code TomoWarp documented by Hall *et al.* (2009); Charalampidou *et al.* (2011, 2014) have demonstrated that 3-D volumetric DIC can effectively map out the geometric complexity of strain localization in porous sandstone. This code is based on a semblance approach initially developed for time-lapse analysis of hydrocarbon reservoirs using 3-D seismic images (Hall 2006). In this study we used TomoWarp to infer the inelastic displacement and strain fields in five hydrostatically and triaxially compressed samples of Majella2.

Before using the TomoWarp code, one has to specify a regular 3-D grid of nodes distributed over the CT image, and a volumetric domain (the ‘correlation window’) centred on each node for the correlation analysis. In the current study, the grid spacing of the nodes was 20 voxels in each direction and the correlation window had a volume of $11 \times 11 \times 11$ voxels³. The displacement field was derived by identifying the 3-D translation that maximizes the cross-correlation of the grey-level data within the correlation window in the undeformed and deformed images at each node. The displacement field so determined is based on a discrete unit (related to the voxel dimension), and therefore a further step determines a subvoxel resolved translation vector based on the maximum of the interpolated correlation coefficient for a range of displacements around the initial integer voxel value. Subsequent calculation of the strain tensor is based on interpolation of the displacements over 8-point cubic elements of neighbouring nodes.

Since it is difficult to visualize the spatial distribution of all six independent strain components, we will characterize the strain field by two parameters (defined in terms of the principal strains $\varepsilon_1, \varepsilon_2$ and ε_3): the volumetric strain $\varepsilon_v = \varepsilon_1 + \varepsilon_2 + \varepsilon_3$, and octahedral shear strain $\gamma_s = \sqrt{2[(\varepsilon_1 - \varepsilon_2)^2 + (\varepsilon_1 - \varepsilon_3)^2 + (\varepsilon_2 - \varepsilon_3)^2]}/3$. These two parameters are directly related to the first strain invariant and the square root of the second deviatoric strain invariant, respectively. Physically the octahedral shear strain corresponds to the engineering shear strain sustained on the octahedral plane (defined by its normal which subtends equal angles with respect to the three principal directions).

3 MACROPORE STATISTICS AND SPATIAL DISTRIBUTION OF MICROPOROSITY

In terms of rock fabric, Majella limestones can be classified according to Dunham (1962) as a calcite-cemented grainstone. It has a modal composition of >99 per cent calcite. Allochems in the limestone make up about half of the bulk rock volume, and they are primarily in the form of rudist fragments. The rest of the solid volume is occupied by cements in the form of bladed sparry calcite cements and microspherules of silica cement. Under the SEM, the larger macropores were observed to have dimensions comparable to the allochems (Fig. 2a), whereas numerous micropores are embedded in the allochems and cemented regions (Fig. 2b). Fig. 2(c) highlights numerous micron-sized micropores that can be found in the periphery of a macropore. For comparison we show in Fig. 2(d) the spatial partitioning of allochems, matrix and porosity in a Majella limestone sample that was mapped manually by Tondi *et al.* (2006) under an optical microscope. The allochems (light areas) are primarily rudist fragments that are quite angular and poorly sorted.

We calculated the total porosity from the density of a vacuum dried sample, assuming a solid composition of 100 per cent calcite with density of 2710 kg m⁻³. The average total porosity of Majella2 limestone so determined is 32.6 per cent, which is slightly larger than the interconnected porosity values of 31 and 30 per cent determined on Majella1 by pycnometer and water saturation techniques, respectively (Baud *et al.* 2009). From 2-D measurements on a scanned image of the thin-section (of an undeformed Majella1 sample of total porosity 30 per cent), the macroporosity was inferred to be 11.4 per cent (Zhu *et al.* 2010; Vajdova *et al.* 2012). The difference between the two would give a microporosity of 19.6 per cent.

3.1 Macroporosity and microporosity

The micro-CT image was segmented into three domains. Voxels in the macropore domain have local porosity of 1, and they occupy 11.4 per cent of the volume. In the intermediate domain, the local porosity ranges from 0 to 1. Using eq. (2) the local porosity in this domain can be inferred (Fig. 3). Its distribution follows an approximately bilinear trend, with significant proportion of the voxels inferred to have local porosities <40 per cent. It should be noted that, in expression (2), we selected I_{void}^* and I_{solid}^* as the limits, and there are other choices one can make and alternative expressions which one can propose for inferring the porosity, and it is a moot question which will give the best approximation (Ji *et al.* 2012).

A 3-D visualization of the grey level distribution is presented in Fig. 4(a). Whereas the solid domain seems to be interconnected, it is not obvious to what extent the macropores (Fig. 4b) and the intermediate domain (Fig. 4c) are interconnected. In Fig. 5 we present five slices of a subvolume, which show many features qualitatively similar to the optical micrographs in Fig. 2. Many of the macropores and solid grains seem to be surrounded by layers of the intermediate domain.

3.2 Geometric characterization of the macropores and microporosity domain

With morphological processing we identified a total of 17 028 macropores with a diversity of geometric shapes. We show in Fig. 6 four selected macropores with sphericity ranging from 0.24 to 0.94. Basically all macropores can be considered as isolated blobs, except for a single one that cuts through the sample thus providing a percolative backbone. This backbone (Fig. 6b) is geometrically complex, has a very low sphericity of 0.04, and occupies a significant portion of the pore space (9.97 per cent porosity).

We present in Fig. 7(a) the equivalent diameter distribution for the macropores. Most of the isolated pores have equivalent diameters less than 100 μm , and there seems to be an overall trend for a more significant proportion of the larger pores to deviate from a spherical geometry. For comparison we show in Fig. 7(b) the data of Vajdova *et al.* (2012), which were obtained on 2-D scanned image of the thin-section of I0-TS. They did not characterize the pore shape, and the equivalent diameter was calculated for a circle with area identical to the projected area of the pore observed on the 2-D section. Both sets of data fall on similar ranges of equivalent diameter, and they follow qualitatively similar trends with number of pores decreasing with increasing diameters. Using stereological concepts (Underwood 1970) and assuming isotropy, the 2-D and

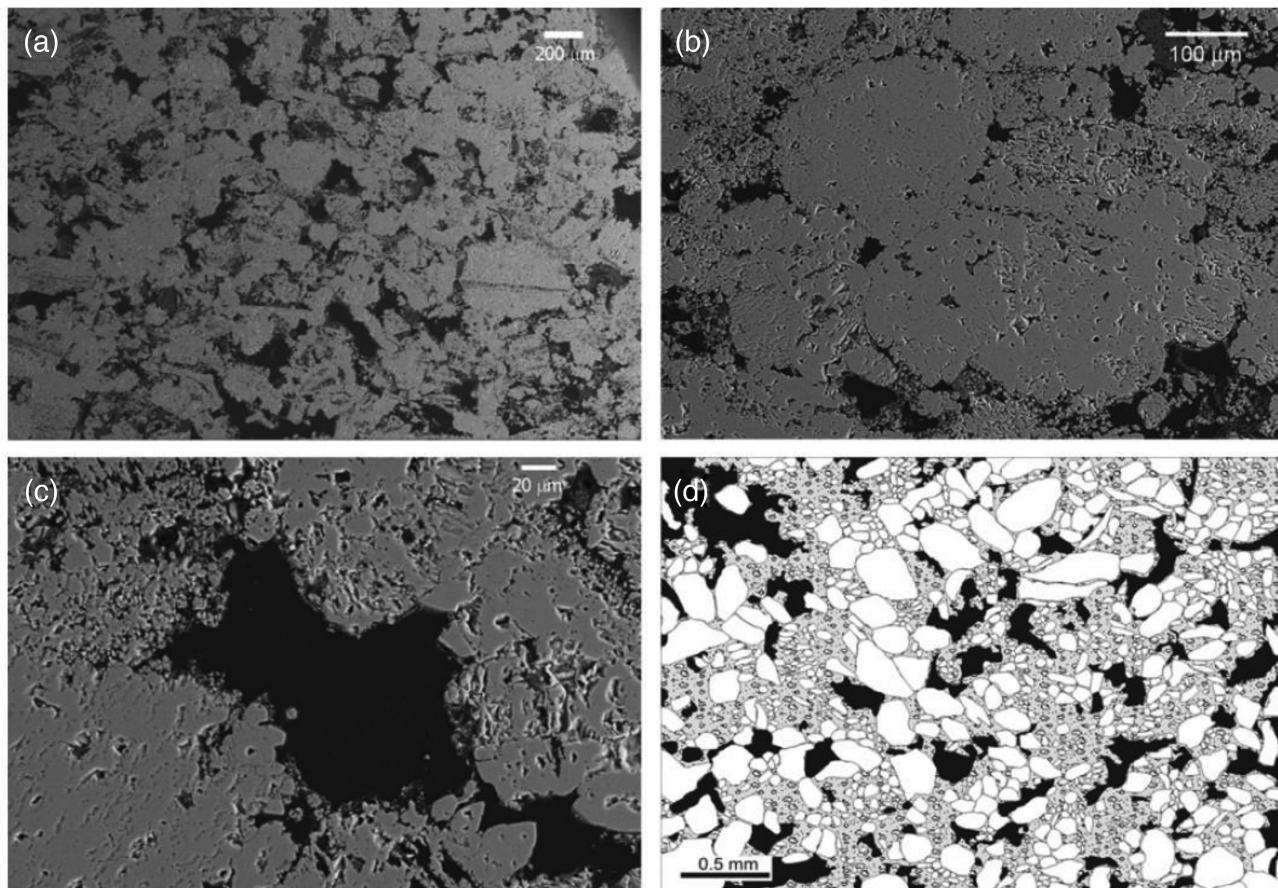


Figure 2. Backscattered SEM images of an intact sample of Majella limestone (sample M0-TS from Vajdova *et al.* 2012). (a) The larger macropores (dark areas) have dimensions comparable to the allochems. (b) Micropores embedded in the allochems and cemented regions. (c) Numerous micropores in the periphery of a macropore. (d) Map performed manually under optical microscope (Tondi *et al.* 2006) showing the partitioning of allochems (rudists), matrix (mostly cement) and porosity in a Majella limestone.

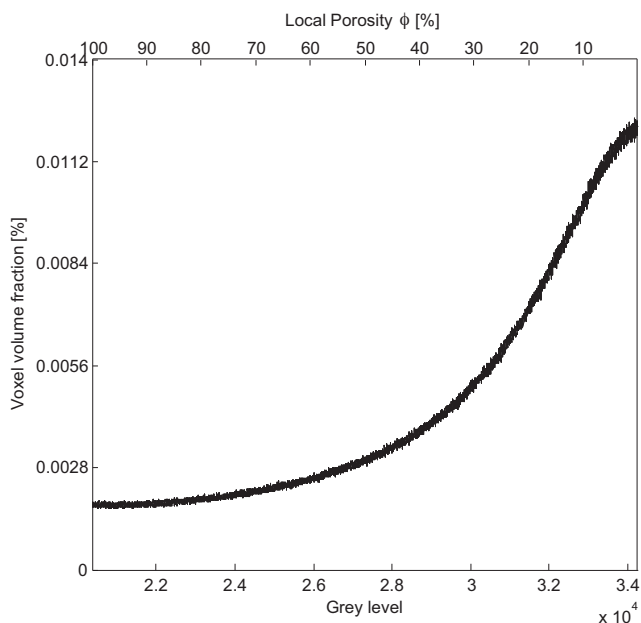


Figure 3. Distribution of microporosity from CT data on intact Majella limestone (smoothed with a $5 \times 5 \times 5$ median filter). Voxel volume normalized to the sample volume as a function of the grey level and of the corresponding inferred local porosity in the intermediate zone.

3-D measurements (of number per unit area n_A and per unit volume n_V) of a system of spherical objects are related by:

$$n_V = \frac{n_A}{\bar{D}}, \quad (5)$$

where \bar{D} denotes the mean diameter of the spherical objects.

Our analysis has revealed significant discrepancy between 2-D and 3-D measurements of pore size statistics of Majella limestone. For example, let us consider equivalent diameters in the range of 33–50 μm . From 2-D measurement the number of macropores per unit area is $n_A \sim 10.5 \text{ mm}^2$ (Fig. 7b), and using a mean diameter of $\bar{D} = 42 \mu\text{m}$, we would expect from (5) that $n_V \sim 250 \text{ mm}^{-3}$. In comparison, a significantly lower value of $n_V = 10\text{--}60 \text{ mm}^{-3}$ was obtained from our micro-CT data (Fig. 7a). It is likely that the discrepancy arises from the existence of a percolative backbone in Majella limestone, which is counted as a single entity in the 3-D analysis, but in 2-D measurement may appear as a multiplicity of isolated macropores that intersect a cross-section and present an unrealistically high value.

For the intermediate domain, our morphological analysis could identify very few isolated clusters of microporosity that altogether occupy <0.2 per cent of the voxel volume in this domain. In other words, the microporosity domain in the limestone sample is basically made up of one interconnected backbone.

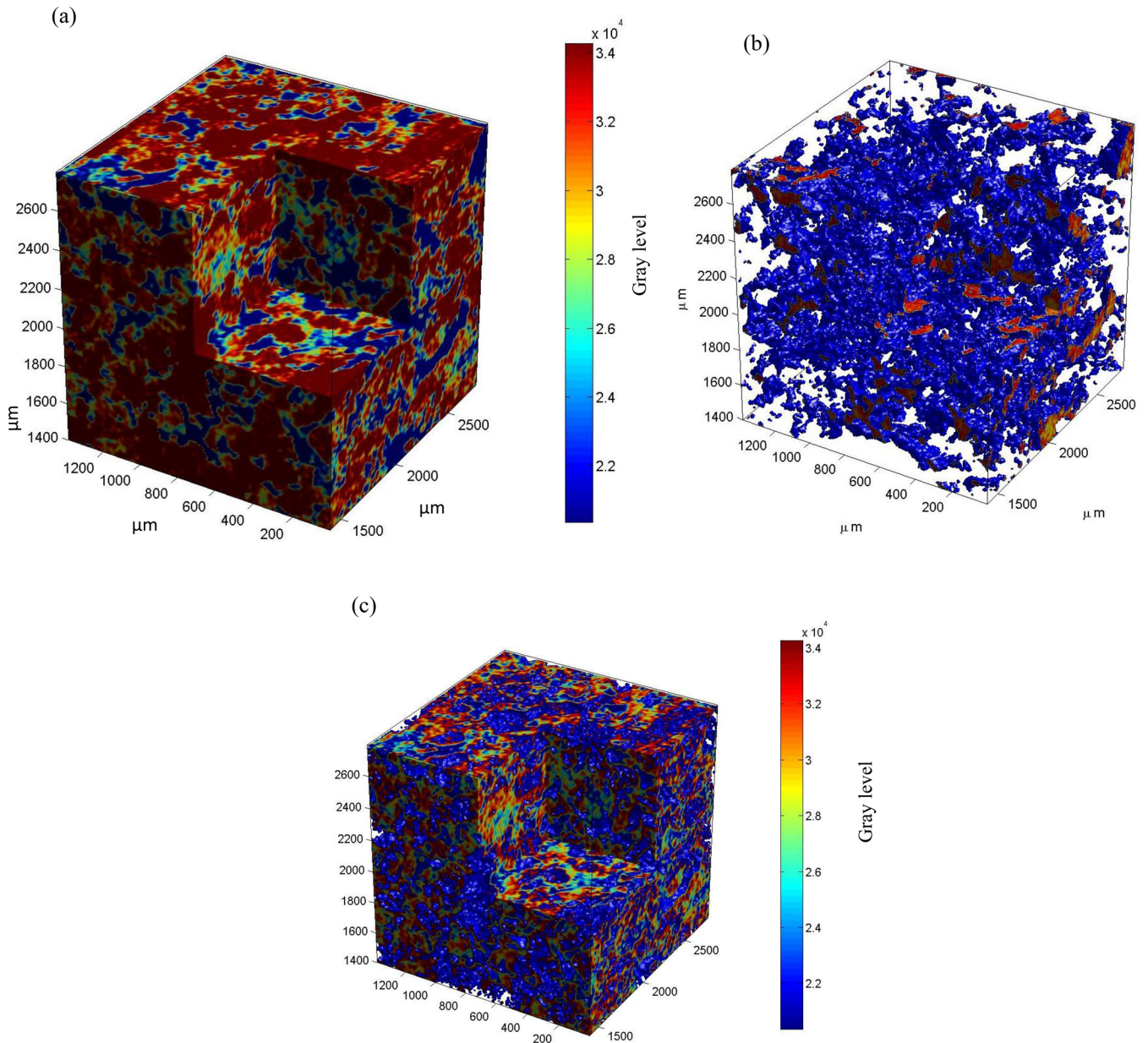


Figure 4. 3-D reconstruction of the intact sample of Majella limestone showing (a) the three identified domains, (b) the macroporosity and (c) the intermediate domain. The cubes represent 1/8 of the whole sample. The CT data were smoothed with a $5 \times 5 \times 5$ median filter.

4 STRAIN LOCALIZATION CHARACTERIZED BY DIC

With decreasing confinement, the failure mode of a porous rock undergoes a transition from delocalized compaction to brittle faulting, with development of shear bands that may be accompanied by dilation or compaction (Bésuelle 2001; Wong & Baud 2012). Dilatancy enhances the local porosity and is very effective in highlighting the contrast in X-ray attenuation between a dilating shear band and its surrounding (e.g. Raynaud *et al.* 1989; Kawakata *et al.* 1999; Bésuelle *et al.* 2003). In contrast, localized compaction is not as effective and the relatively subtle contrast between a compacted zone and its surrounding is not readily resolved by visualization of the primary CT data even at high resolution.

4.1 Mechanical data and microstructural observation

For the presentation of the mechanical data, we have adopted the convention that compressive stresses and compactive strains (i.e. shortening and porosity decrease) are positive. The maximum and minimum principal stresses will be denoted by σ_1 and σ_3 , respectively. The mechanical data for Majella2 are typical of the brittle-ductile transition in porous rocks. Strain softening was observed at 5 and 10 MPa (Fig. 8a). With increasing confining pressure, the failure mode became ductile with more pronounced strain hardening for the sample deformed at the highest confining pressure (25 MPa). Shear-enhanced compaction was observed in agreement with the Majella1 data of Baud *et al.* (2009) (Fig. 8b). We compiled the yield stresses (solid symbols) at the onset of inelastic compaction of our Majella2

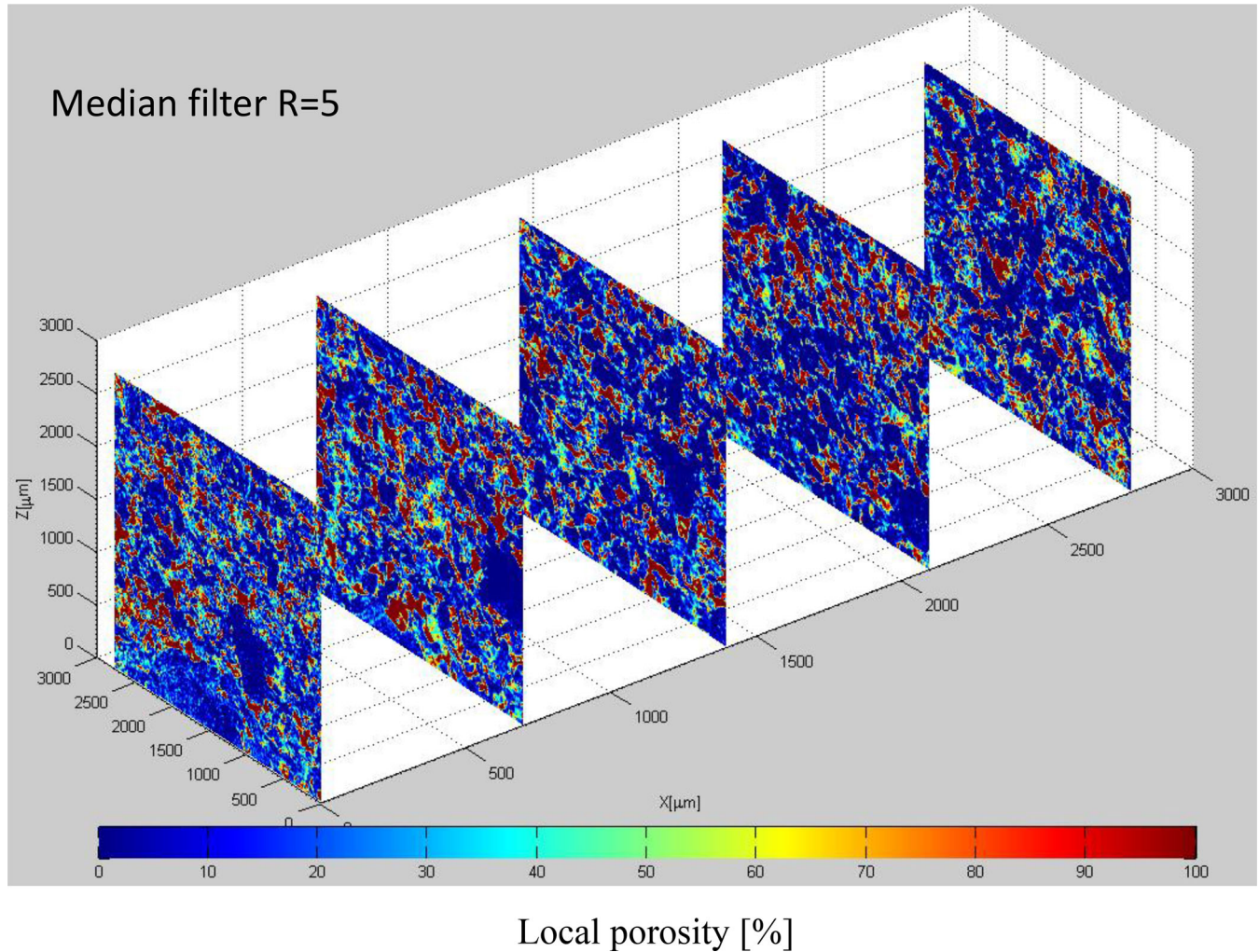


Figure 5. Five slices from a subvolume of the intact sample of Majella limestone showing the partitioning between solid grains, macroporosity and the intermediate zone dominated by microporosity.

samples, as well as the Majella1 data (open symbols) of Baud *et al.* (2009) (Fig. 9). The two sets of data are qualitatively similar in that each maps out an elliptical yield cap. However, it should be noted that overall Majella2 seems significantly weaker, possibly because of its higher porosity and that our samples were cored perpendicular to bedding, whereas the samples of Baud *et al.* (2009) were cored parallel to bedding.

That failure at 5 and 10 MPa was accompanied by stress drops would suggest development of shear localization. However, visual inspection of the failed samples did not indicate any strain localization features, and likewise for the two samples failed at higher pressures of 15 and 25 MPa. After the failed samples had been scanned, they were cut and thin sections prepared for optical microscopy and SEM observations. In each sample, a few isolated patches made up of crushed grains could be discerned under very high magnification. After we had scrutinized the thin sections in detail under the SEM, we were not able to reach any conclusions based on the rather subtle microstructure as to whether the damage had indeed coalesced into shear bands. In contrast, a more definitive scenario emerged from DIC analysis of the two CT images acquired for each sample before and after a deformation experiment.

4.2 Strain localization and spatial distribution of strain from DIC

In each of the five samples, the 2-D strain distributions on an axial plane (Fig. 10) indicate that overall the volumetric strain is compressive (positive), and strain magnitudes from the DIC analysis are comparable to the maximum strains attained in the mechanical tests, which were on the order of 1 per cent (Fig. 8). Whereas the inelastic deformation seems delocalized in the hydrostatically compacted sample, its spatial distribution in the four triaxially compressed samples suggests strain localization, even though the volumetric strain contrast is quite weak and not useful for constraining definitively the localized features.

Shear strain distributions in the four triaxially compressed samples show significant heterogeneity, suggestive of strain localization. The two samples deformed at confining pressures of 5 and 10 MPa failed with strain softening. Near one end of either sample, a band associated with enhanced shear strain can readily be identified. The axial planes in these two figures were oriented to be approximately perpendicular to the bands. The band orientations are at high angles ($>45^\circ$) with respect to the maximum compression direction. Given

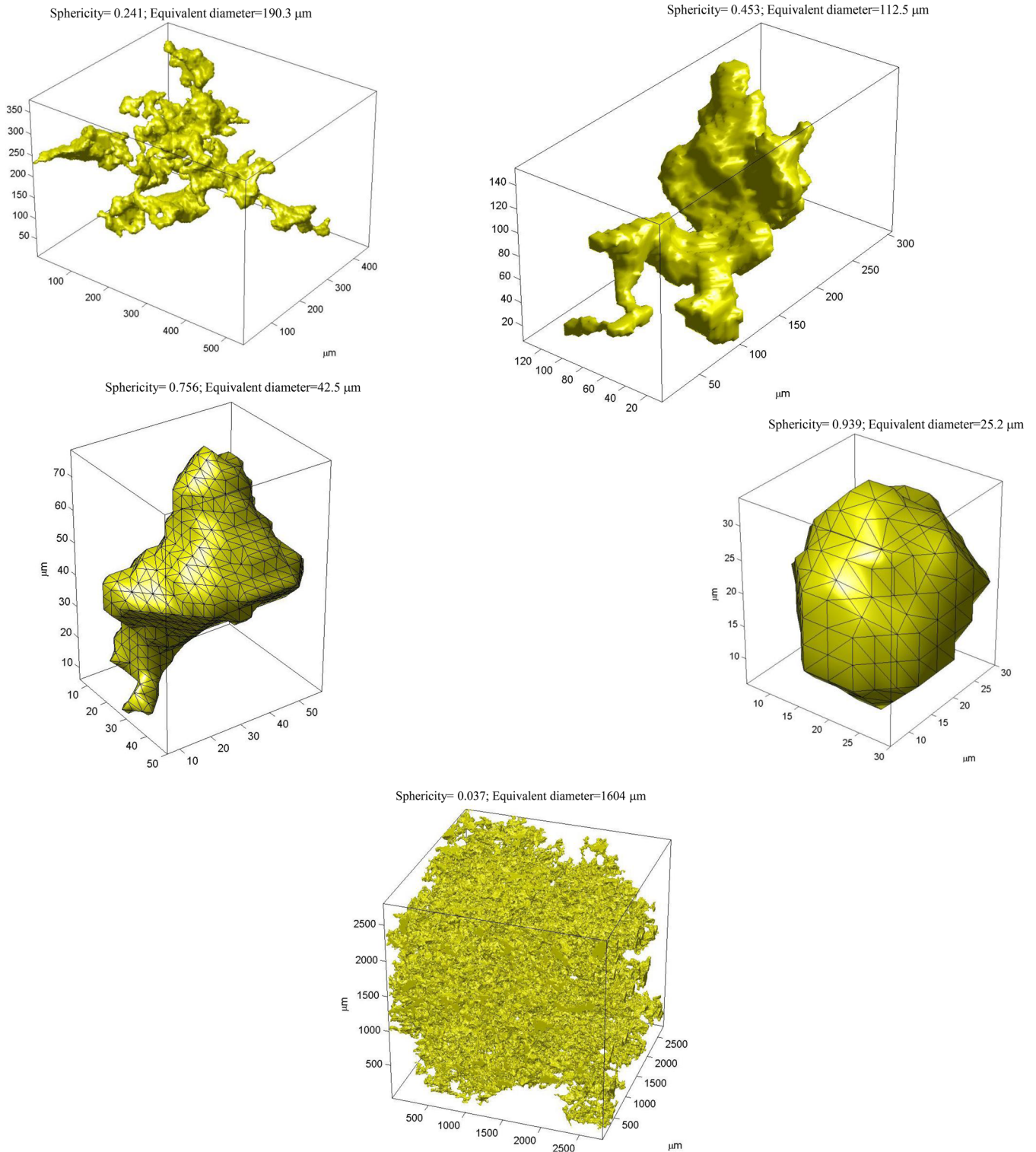


Figure 6. (a) Macropores in an intact sample of Majella limestone mapped out using the marching cubes algorithm. The sphericity ψ and the equivalent diameter D are given for each macropore. (b) Percolative backbone of complex geometry ($\psi = 0.04$), and occupying 9.97 per cent of the porosity.

these observations, the mode of localization in these two samples can be categorized as high-angle compacting shear bands. Although we have DIC data on the displacement vectors, the spatial distribution of their orientations in the vicinity of these bands is rather complex and not easily visualized for elucidating the kinematics of shear localization.

In the other two samples deformed at pressures of 15 and 25 MPa, zones apparently made up of multiple strands of closely spaced tortuous bands with enhanced shear strain have developed. Had we not imaged the third dimension, it would be difficult to differentiate whether these bands are inclined or subperpendicular to the maximum compression direction,

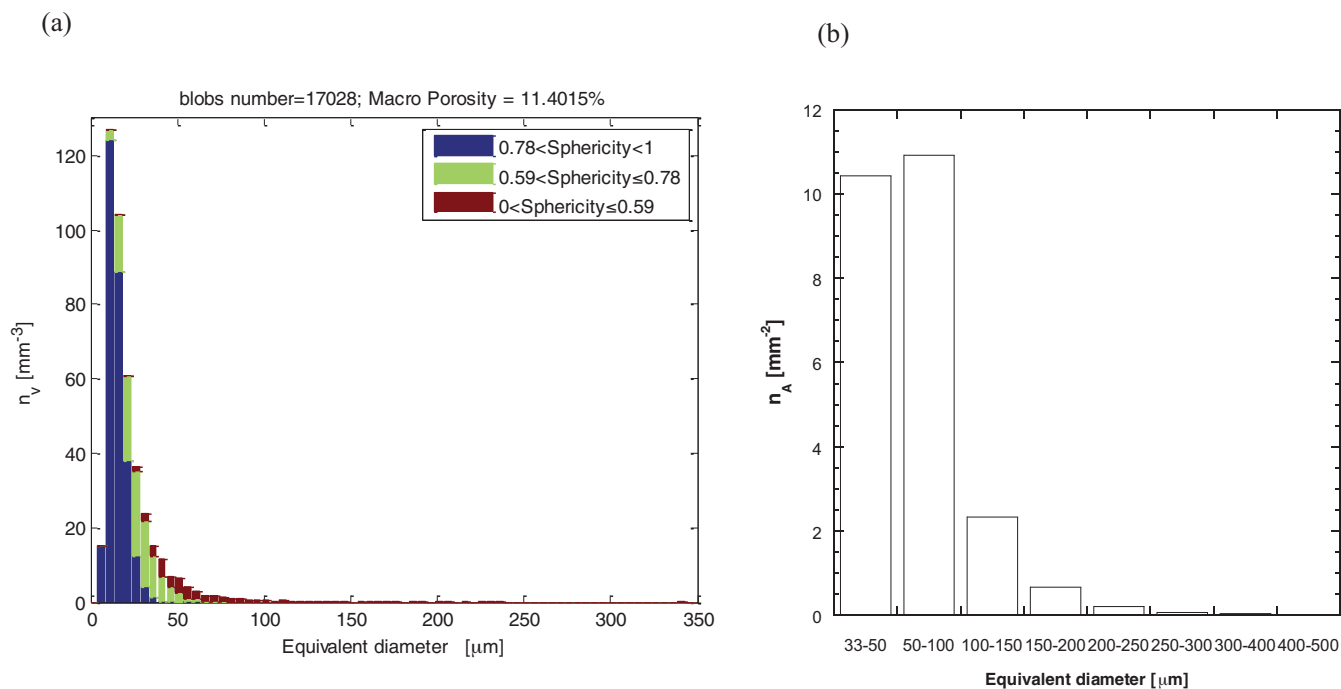


Figure 7. (a) Distribution of equivalent diameter of the macropores identified by morphological analysis in intact Majella limestone. The number of pores per unit volume n_V is plotted versus the equivalent diameter D . The macropores were divided into three groups according to their sphericity: sphericity > 0.78 (blue), $0.59 < \text{sphericity} < 0.78$ (green), $0 < \text{sphericity} < 0.59$ (brown). (b) Size distribution of pores resolved from a scanned image at a resolution of 2400 dpi (Vajdova *et al.* 2012). The number of pores per unit area n_A is plotted versus equivalent diameter.

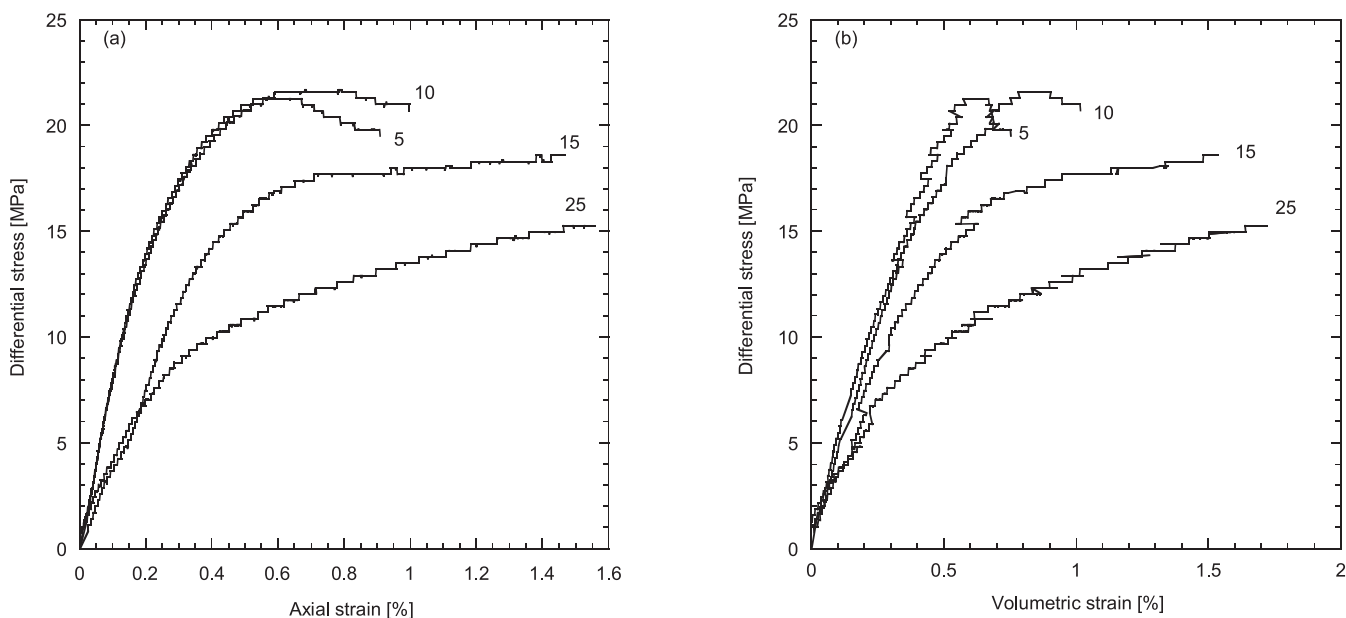


Figure 8. (a) Principal stress difference $\sigma_1 - \sigma_3$ versus axial strain for four samples of Majella limestone triaxially compressed between 5 and 25 MPa of confining pressure. (b) Differential stress as a function of volumetric strain for the same samples. The confining pressures are indicated by numbers (in MPa) next to the each curve.

which would correspond to shear bands or compaction bands, respectively.

To highlight the 3-D development of failure mode, we will present in the next four figures (Figs 11–15) selected serial sections (with colour-coded shear strain) on planes perpendicular to the sample axis. For each sample, we also selected an appropriate threshold for binarizing the shear strain data. The binarized data are then

presented in a volumetric visualization, such that the solid voxels correspond to regions of relatively high strain (above the threshold).

Data for the hydrostatically compacted sample (Fig. 11) corroborate the 2-D observation (Fig. 10) that strain localization is absent. For the sample deformed at 5 MPa pressure, the serial sections indicate development of a shear band that cut through the sample from one end (Fig. 12). The local strains within the band are

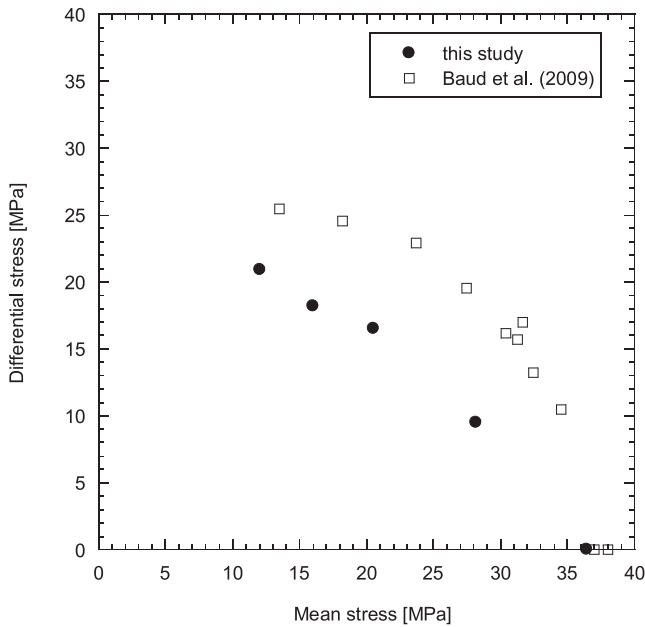


Figure 9. Initial yield stress C^* for (open squares) Majella1 (Baud *et al.* 2009) and (black circles) Majella2 (this study).

significantly higher than the global strain and the binary shear strain data reveal that the orientation of the band is 57° with respect to the major principal stress σ_1 (Fig. 12d). An analogous shear band has also developed in the sample deformed at 10 MPa (Fig. 13), but with two differences in its geometry. First, the angle (with respect to the maximum compression direction) is somewhat smaller (Fig. 13d). Secondly, the serial sections (Fig. 13a) show that the band in this sample seems to deviate more from a planar geometry, with a curvature that mimics the outer surface of the cylindrical sample.

Serial sections and 3-D visualization of the strain field in the sample deformed at 15 MPa (Fig. 14) indicates a different failure

mode: the development of multiple strands of closely spaced high-angle shear bands. A section cut in the binarized data (Fig. 14d) suggests that the average orientation of these bands with respect to the major principal stress is about 53° . As for the sample deformed at 25 MPa, the 2-D sections in Fig. 15(a) do not quite support a failure mode involving compaction bands, which would be manifested by relatively high strains that pervade one or more of the serial sections. The strain distribution strongly suggests that failure in this sample had also involved the development of numerous high-angle shear bands oriented at angles between 53 and 66° to the maximum compression direction (Fig. 15d).

5 DISCUSSION

5.1 Pore structure of limestone and implications on hydraulic and mechanical properties

Due to the geometric complexity of its pore space, standard techniques for CT imaging of porous siliciclastic rock are not directly applicable to a carbonate rock. Hence most investigations of the pore structure and damage development in porous carbonate rocks have been done on 2-D thin-sections, synthesizing observations on different scales using the optical microscope and SEM. In this study, we have demonstrated the feasibility and usefulness of two CT techniques for characterizing the pore structure and development of strain localization in a porous limestone.

The first technique allows us to extract 3-D information from micro-CT data on the partitioning of porosity and pore size statistics in Majella limestone, with constraints from microstructural observations on 2-D sections (Zhu *et al.* 2010; Vajdova *et al.* 2012). Our results complement the earlier study of Ji *et al.* (2012), who reported similar partitioning of the pore space in Indiana limestone with a significantly lower porosity. Together these studies imply that a dual porosity model is necessary for analysing the mechanical and transport behavior of porous carbonate rock.

Our morphological analysis of the micro-CT images shows that both the solid and intermediate domains in Majella limestone are

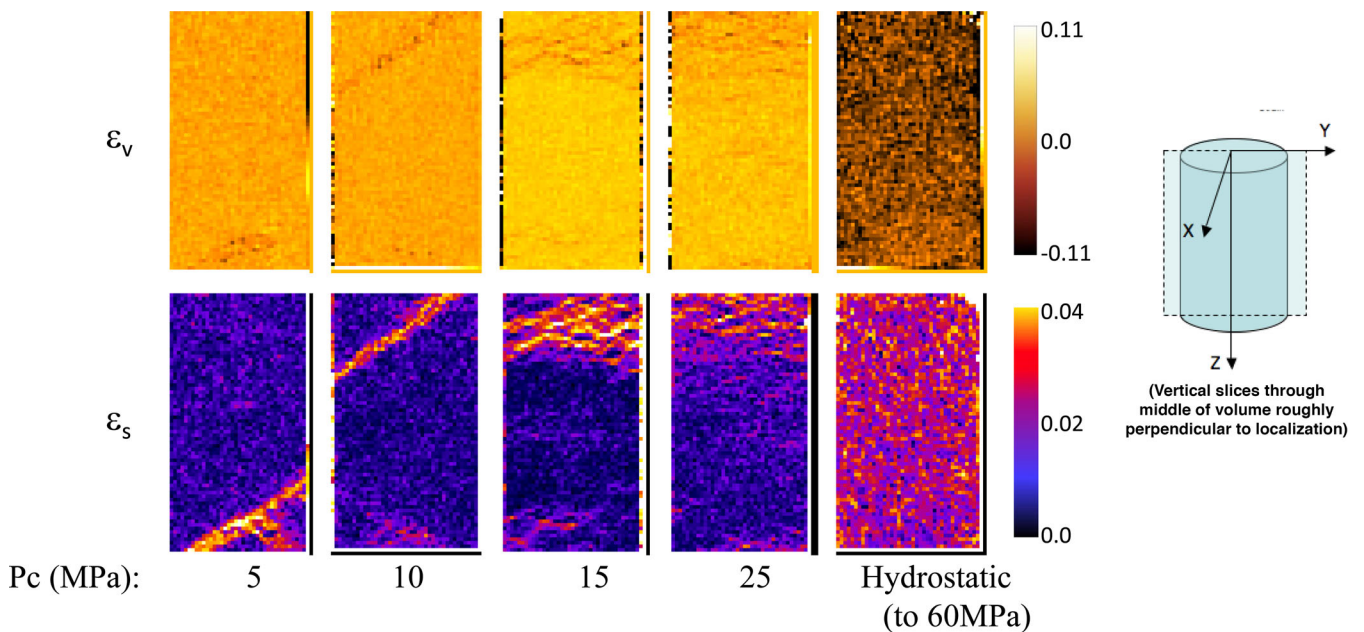


Figure 10. 2-D strain distributions on an axial plane of each of the five deformed samples of Majella limestone analysed by DIC. The volumetric strain (top panel) and the octahedral shear strain (bottom panel) are presented on the figure.

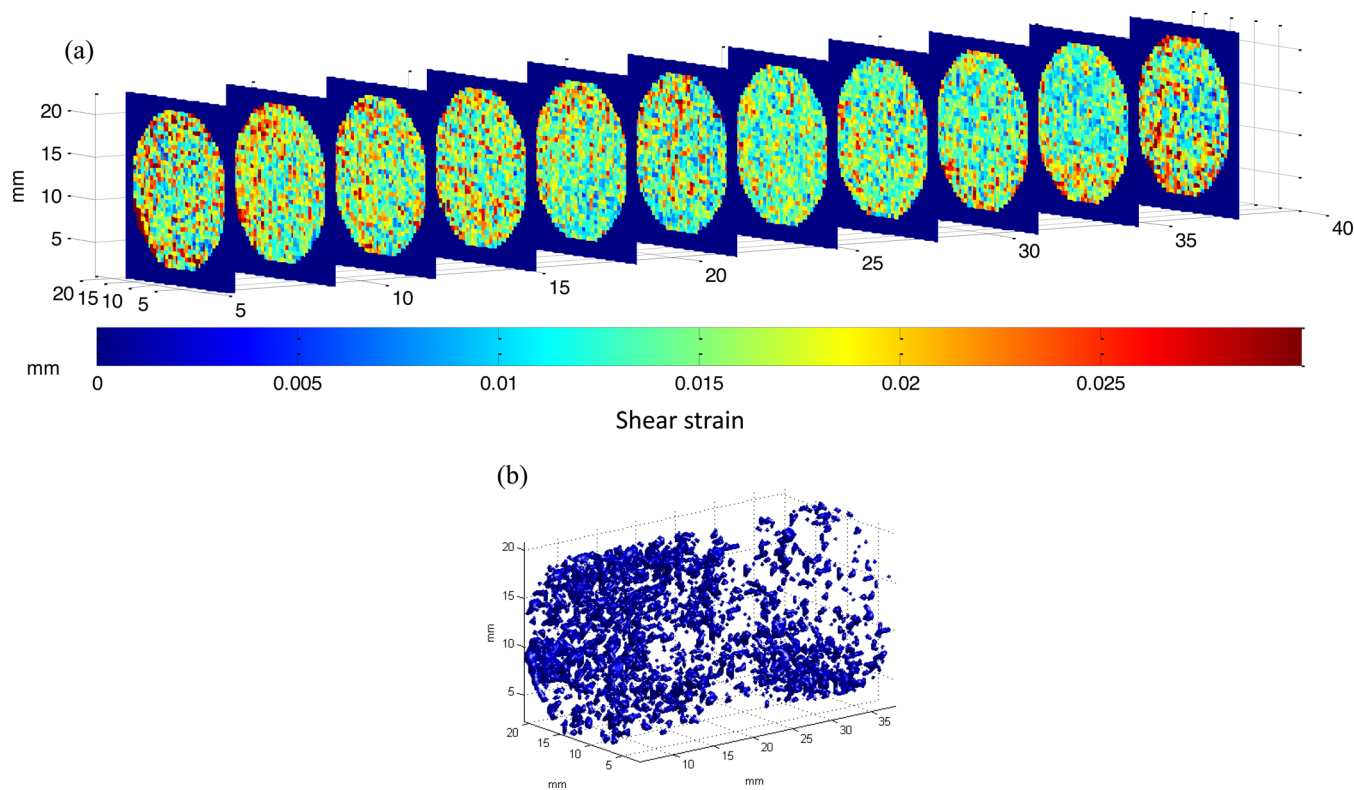


Figure 11. (a) Selected serial sections (with colour-coded shear strain) of the sample of Majella limestone deformed hydrostatically up to 60 MPa of confining pressure. The sections are from planes perpendicular to the sample axis. (b) Binarized shear strain data for the same sample presented in a volumetric visualization, such that the solid voxels correspond to regions of relatively high strain (above a set threshold).

basically interconnected. Mercury injection data of Baud *et al.* (2009) indicate that the micropores are connected by throats with micron- and submicron-sized apertures. Our study also shows that macroporosity in Majella limestone has a percolative backbone (Fig. 6b) that may contribute to significant enhancement of its permeability. Recently there have been a number of attempts to simulate limestone permeability (Al Kharusi & Blunt 2007; Okabe & Blunt 2007; Bauer *et al.* 2011). Implicit in many models is the assumption that the flow in the macropores and micropores can be considered as two networks in parallel. Accordingly to our morphological analysis, such an assumption is appropriate for Majella limestone with percolative backbones for both types of porosity, but its validity is questionable in the case of the less porous Indiana limestone (Ji *et al.* 2012). How to realistically simulate the permeability in the latter case (with isolated macropores connected to an interconnected microporosity domain) is a challenging question that warrants further systematic investigation.

As for mechanical deformation, recent studies concluded that macropores and micropores have fundamentally different influences on the elastic properties (Baechle *et al.* 2008; Knackstedt *et al.* 2009) and compaction (Ji *et al.* 2012; Vajdova *et al.* 2012) of porous limestone. Inelastic compaction develops by macropore collapse, but the micropores also play an important role in controlling the damage development in the vicinity of a macropore, as postulated by the dual porosity model of Zhu *et al.* (2010). Although they are interconnected, it is likely that the macropores are connected by relatively narrow throats that may be readily closed mechanically under high confinement, and their mechanical responses would then be similar to those of isolated pores. In that case, we expect the micromechanics of inelastic compaction to be qualitatively similar in limestones over a broad range of porosity.

5.2 Development of strain localization in the transitional regime

The second technique undertaken in this study is DIC analysis of the failure mode in relation to the transition from brittle faulting to cataclastic flow. In the transitional regime, shear bands may develop at an angle (relative to the maximum compression direction) significantly larger than that in the brittle faulting regime (Paterson & Wong 2005; Wong & Baud 2012). The diversity of failure modes have been documented in porous sandstone by systematic microstructural observations (e.g. Baud *et al.* 2004) and CT imaging (e.g. Charalampidou *et al.* 2011). However, there is a paucity of data regarding the failure mode of porous limestone, and our study fills in this gap.

As noted earlier the damage associated with strain localization in Majella limestone is subtle and not easily resolvable under optical microscope or SEM. Experience of Baud *et al.* (2009) indicates that deforming the samples to higher strain would not have improved the contrast. These microstructural observations indicate quite limited development of microcracking and pore collapse, and absence of clustering or coalescence of these types of damage. It seems that inelastic deformation in the transitional regime involves a third mechanism. A possible candidate is the relative rotation of allochems accommodated by shear slip along interfaces with the cements. Permanent deformation induced by such a mechanism would be too subtle to detect under the microscope. It is also unclear how such deformation is partitioned between the macroporosity and microporosity.

Our first application of 3-D-volumetric DIC to a very porous limestone has demonstrated the feasibility of mapping out such subtle development of strain localization. This is encouraging and

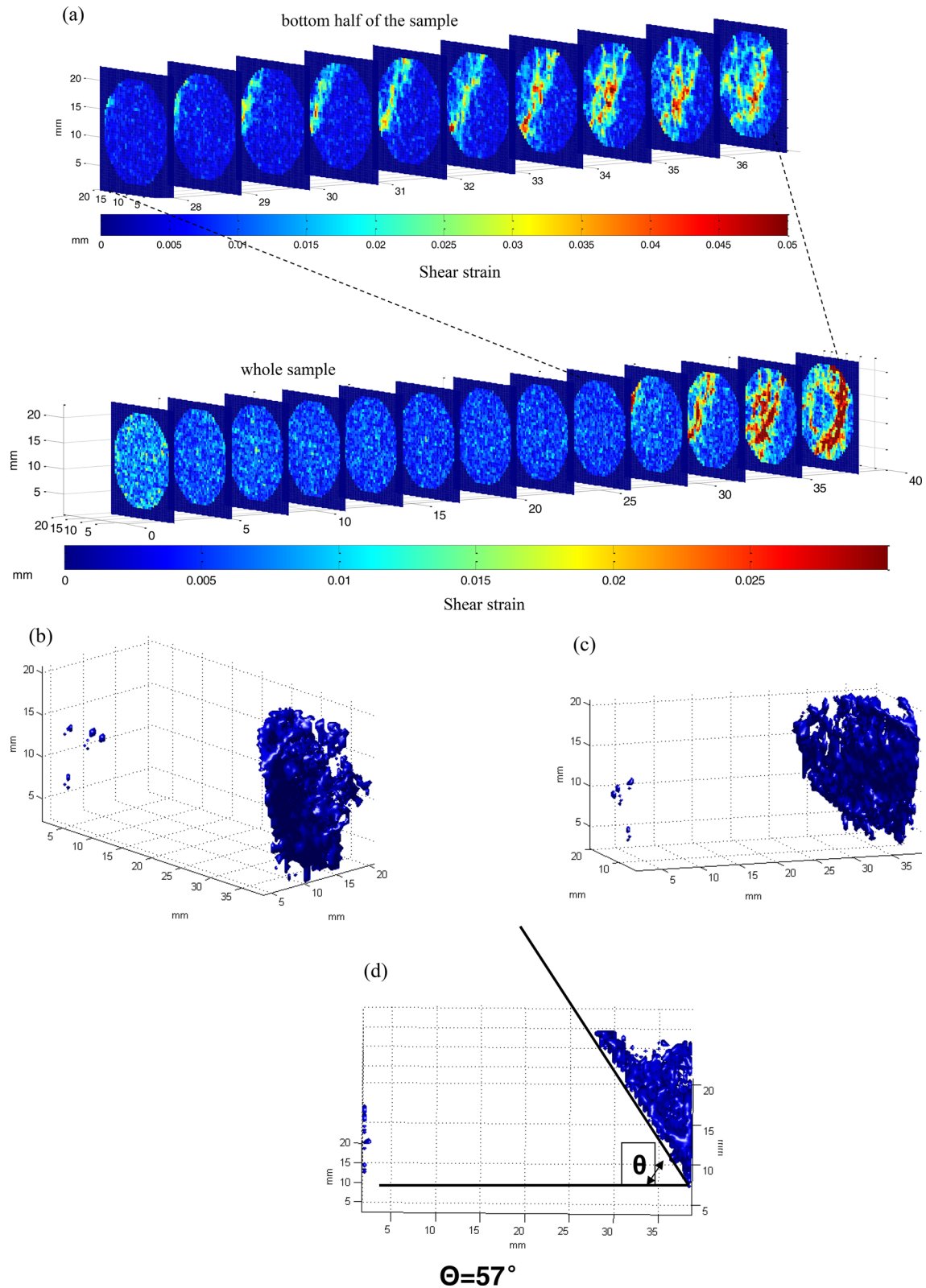


Figure 12. (a) Selected serial sections (with colour-coded shear strain) of the sample of Majella limestone triaxially deformed at a confining pressure of 5 MPa. The sections are from planes perpendicular to the sample axis. (b) and (c) Binarized shear strain data for the same sample presented in a volumetric visualization, such that the solid voxels correspond to regions of relatively high strain (above a set threshold). (d) Section of the binarized data showing a shear band oriented at 57° with respect to the major principal stress.

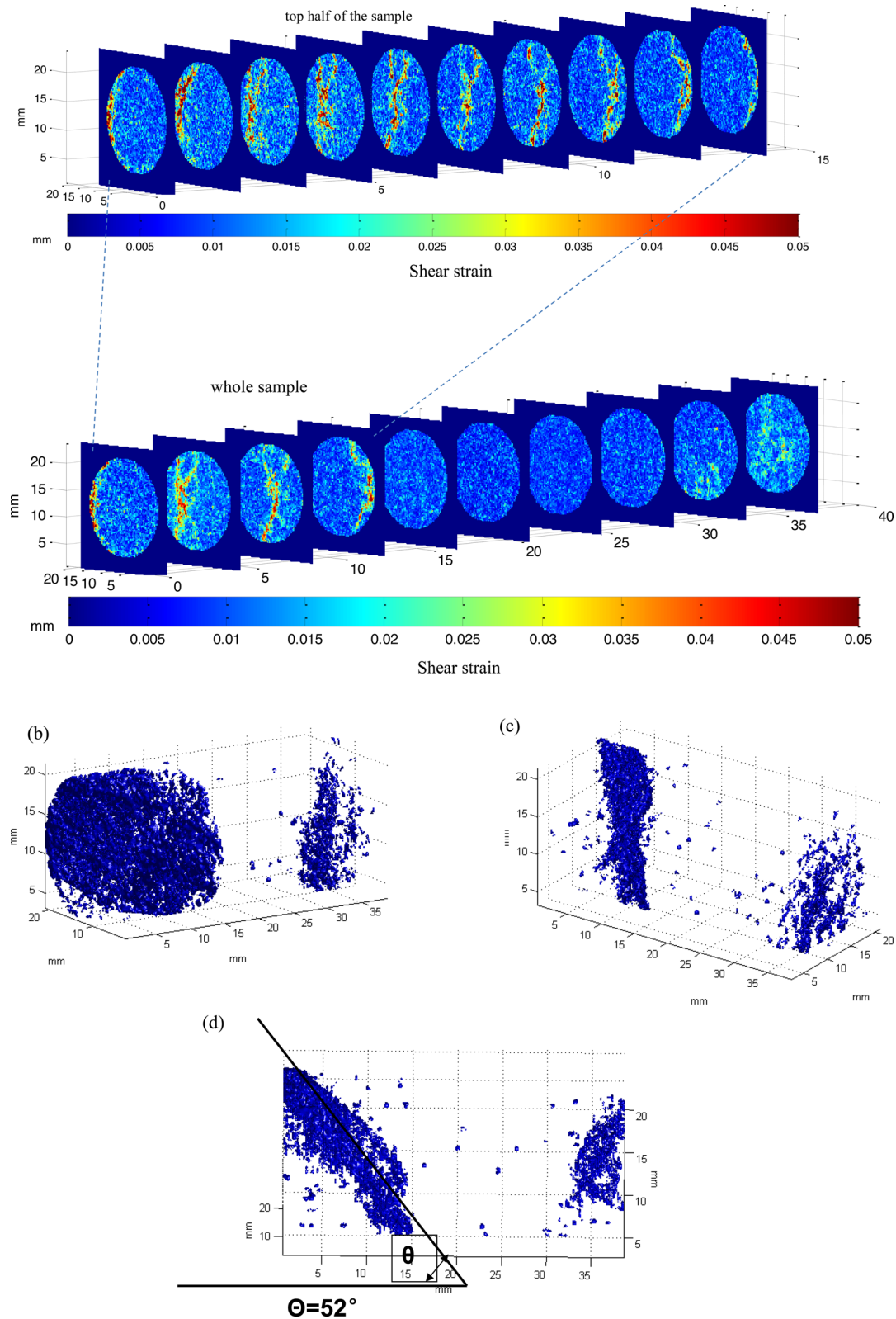


Figure 13. (a) Selected serial sections (with colour-coded shear strain) of the sample of Majella limestone triaxially deformed at a confining pressure of 10 MPa. The sections are from planes perpendicular to the sample axis. (b) and (c) Binarized shear strain data for the same sample presented in a volumetric visualization, such that the solid voxels correspond to regions of relatively high strain (above a set threshold). (d) Section of the binarized data showing a shear band oriented at 52° with respect to the major principal stress.

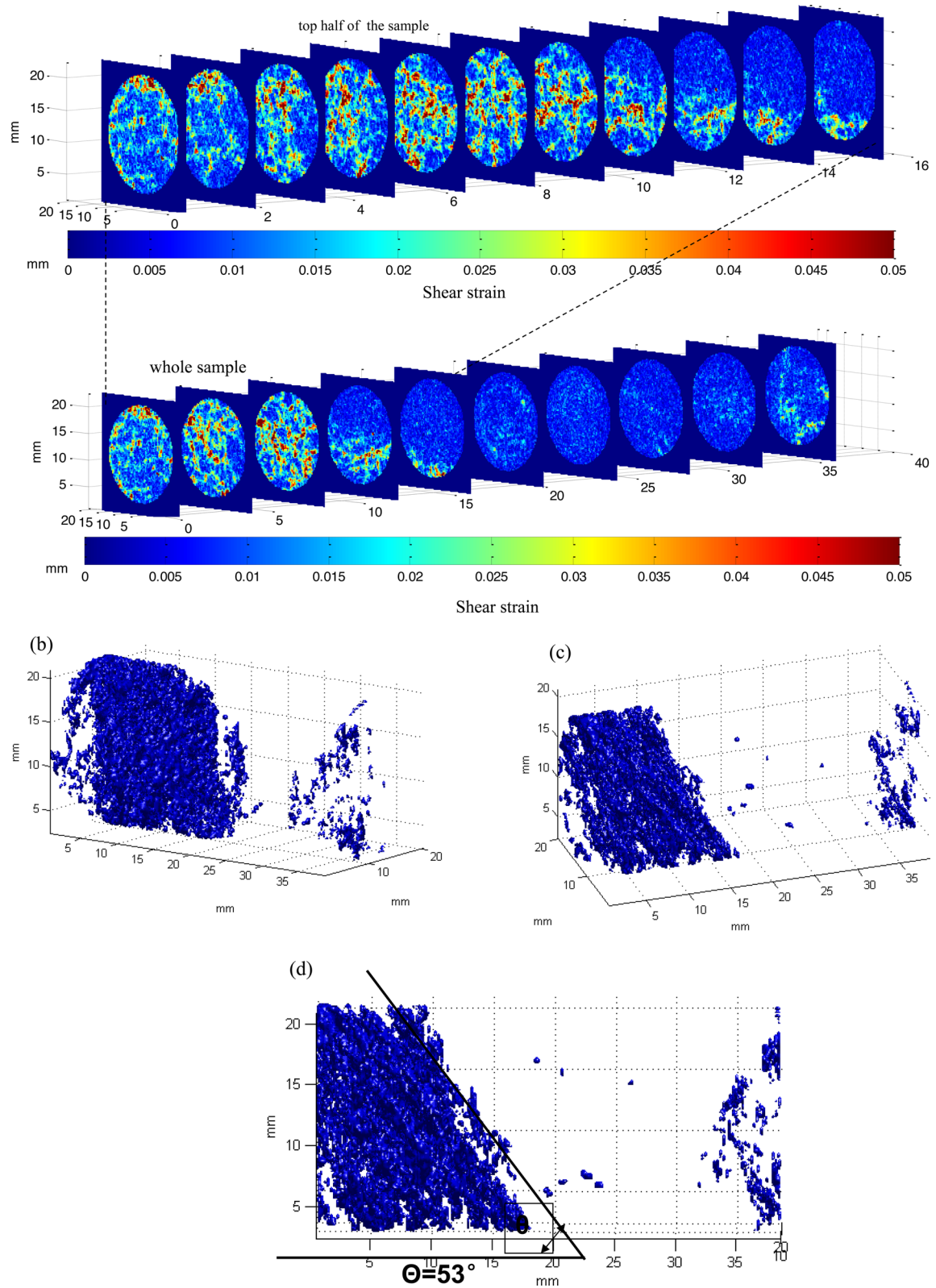


Figure 14. (a) Selected serial sections (with colour-coded shear strain) of the sample of Majella limestone triaxially deformed at a confining pressure of 15 MPa. The sections are from planes perpendicular to the sample axis. (b) and (c) Binarized shear strain data for the same sample presented in a volumetric visualization, such that the solid voxels correspond to regions of relatively high strain (above a set threshold). (d) Section of the binarized data showing multiple strands of closely spaced high-angle shear bands with an average orientation of 53° with respect to the direction of major principal stress.

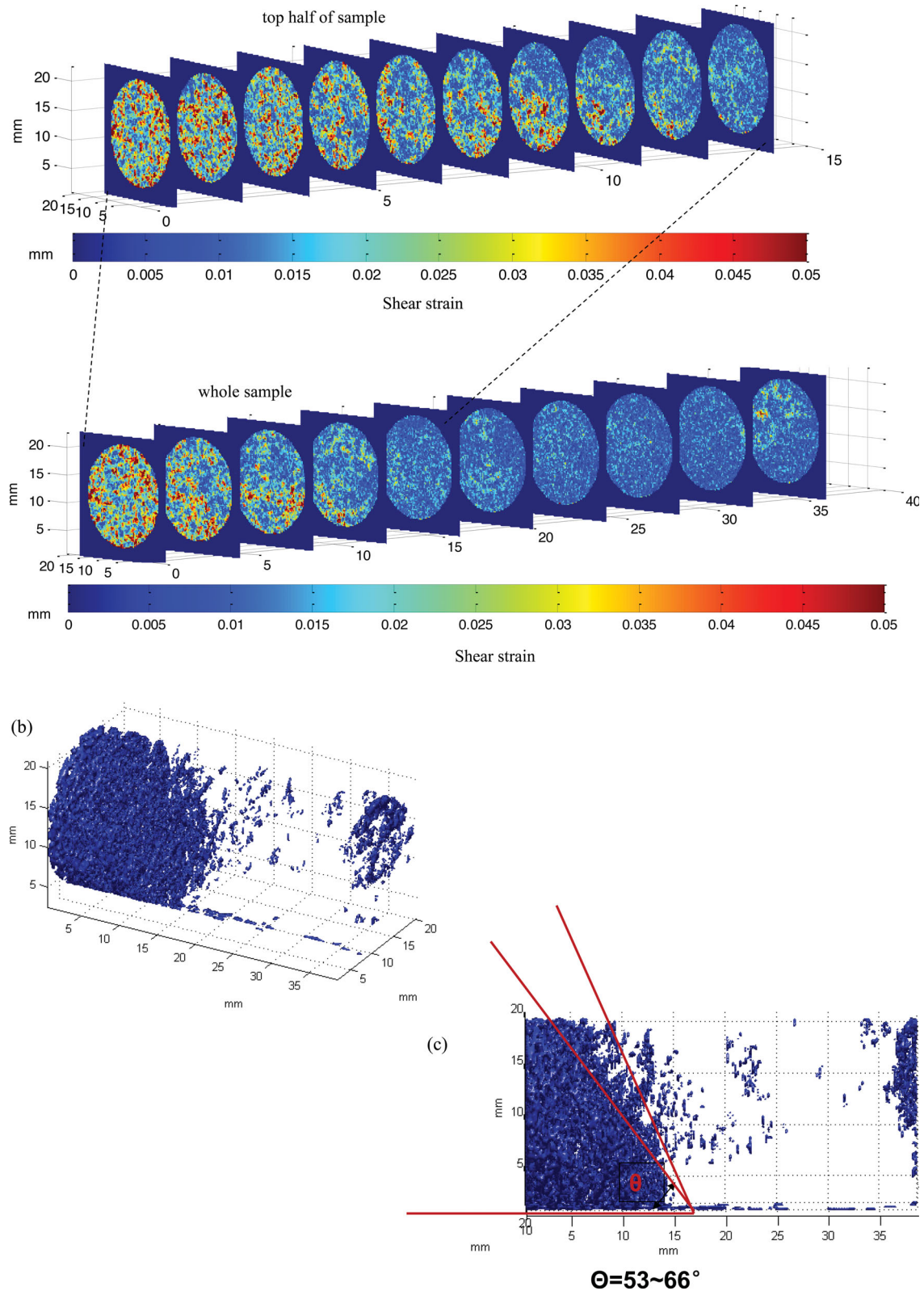


Figure 15. (a) Selected serial sections (with colour-coded shear strain) of the sample of Majella limestone triaxially deformed at a confining pressure of 25 MPa. The sections are from planes perpendicular to the sample axis. (b) Binarized shear strain data for the same sample presented in a volumetric visualization, such that the solid voxels correspond to regions of relatively high strain (above a set threshold). (c) Section of the binarized data showing multiple strands of closely spaced shear bands at angles between 53 and 66° to the maximum compression direction.

DIC promises to be an effective imaging tool for strain localization in other carbonate rocks over a broad range of porosity. Our study demonstrates that strain localization may develop very early at relatively small strains of ~1 per cent, in both the brittle faulting and transitional regimes. The DIC analysis indicates that the localized strains are primarily in the forms of shear and compaction. These observations place useful constraints on the theoretical analysis of strain localization (Bésuelle & Rudnicki 2004).

Our DIC analysis has revealed the structure of high-angle compacting shear bands in the transitional regime, and to our knowledge this is the first systematic observation in a porous carbonate rock. Our DIC data indicate an increase of geometric complexity with increasing confinement - from a planar shear band, to a curvilinear band, and ultimately a diffuse multiplicity of bands, before shear localization is inhibited as the failure mode completes the transition to delocalized cataclastic flow. It should be noted that a somewhat similar scenario in failure mode has been reported in porous siliciclastic rock (e.g. Baud *et al.* 2004), with one key difference in that compaction band as a failure mode in porous limestone has only been observed in a few isolated studies (see, for example Cilona *et al.* 2014). Why compaction bands can readily develop in a number of porous sandstones but seem to be generally inhibited in porous limestones remain an intriguing question that warrants further systematic investigation.

6 CONCLUSION

We have demonstrated the feasibility of two CT techniques for characterizing the 3-D pore geometry and mode of mechanical failure in a porous limestone. Segmentation of the micro-CT images has provided useful insights into the partitioning of porosity and pore size statistics in Majella limestone. Morphological analysis of the images shows that both the solid and microporosity domains are basically interconnected. Furthermore, the macroporosity domain has a percolative backbone that may contribute to significant enhancement of its permeability. For mechanical deformation, recent studies concluded that macropores and micropores have fundamentally different influences on the elastic and inelastic properties, and our new data suggest that the micromechanical processes are qualitatively similar in limestones over a broad range of porosity. A dual porosity model is necessary for analysing the mechanical and transport behaviours of porous carbonate rock.

The use of 3-D-volumetric DIC has allowed us to map out the subtle development of strain localization associated with the transition from brittle faulting to cataclastic flow in Majella limestone. Our observations show that strain localization may develop at relatively small strains of ~1 per cent, in both the brittle faulting and transitional regimes. The localized deformation involves both shear and compaction. Our DIC analysis has elucidated the geometric complexity of compacting shear bands in the transitional regime, which evolve with increasing confinement from a planar shear band, to a curvilinear band, and ultimately a diffuse multiplicity of bands.

ACKNOWLEDGEMENTS

We thank the editor, Peter Eichhubl and an anonymous reviewer for their comprehensive reviews of the manuscript. We have also benefited from discussions with Antonino Cilona, Emanuele Tondi and Sergio Vinciguerra. This research was partially supported by the Office of Basic Energy Sciences, Department of Energy un-

der grant DE-SC0004118, and by the National Science Foundation under grant EAR-1044967, by the French Centre de la Recherche Scientifique (CNRS) under a PICS grant and by the Procure collaborative program (project 30805PM). Yuntao Ji was partially funded by the Basic Scientific Funding of Chinese National Nonprofit Institutes (IGCEA1313).

REFERENCES

- Al Kharusi, A.S. & Blunt, M.J., 2007. Network extraction from sandstone and carbonate pore space images, *J. Petrol. Sci. Eng.*, **45**, 41–46.
- Anselmetti, F.S., Luthi, S. & Eberli, G.P., 1998. Quantitative characterization of carbonate pore systems by digital image analysis, *AAPG Bull.*, **82**, 1815–1836.
- Antonellini, M.A., Aydin, A. & Pollard, D.D., 1994. Microstructure of deformation bands in porous sandstones at Arches National-Park; Utah, *J. Struct. Geol.*, **16**, 941–959.
- Arns, C.H., Knackstedt, M.A., Val Pinczewski, W. & Martys, N.S., 2004. Virtual permeametry on microtomographic images, *J. Petrol. Sci. Eng.*, **45**, 41–46.
- Aydin, A. & Johnson, A.M., 1978. Development of faults as zones of deformation bands and as slip surfaces in sandstone, *Pure appl. Geophys.*, **116**, 931–942.
- Aydin, A., Borja, R.I. & Eichhubl, P., 2006. Geological and mathematical framework for failure modes in granular rock, *J. Struct. Geol.*, **28**, 83–98.
- Baechele, G.T., Colpaert, A., Eberli, G.P. & Weger, R.J., 2008. Effects of microporosity on sonic velocity in carbonate rocks, *Leading Edge*, **27**(8), 1012–1018.
- Bastawros, A.F., Bart-Smith, H. & Evans, A.G., 2000. Experimental analysis of deformation mechanisms in a closed-cell aluminum alloy foam, *J. Mech. Phys. Solids*, **48**, 301–322.
- Baud, P., Klein, E. & Wong, T.-f., 2004. Compaction localization in porous sandstones: spatial evolution of damage and acoustic emission activity, *J. Struct. Geol.*, **26**, 603–624.
- Baud, P., Vinciguerra, S., David, C., Cavallo, A., Walker, E. & Reuschlé, T., 2009. Compaction and failure in high porosity carbonates: mechanical data and microstructural observations, *Pure appl. Geophys.*, **166**, 869–898.
- Bauer, D., Youssef, S., Han, M., Bekri, S., Rosenberg, E., Fleury, M. & Vizika, O., 2011. From microcomputed tomography images to resistivity index calculations of heterogeneous carbonates using a dual-porosity pore-network approach: influence of percolation on the electrical transport properties, *Phys. Rev. E*, **84**, 011133.
- Bay, B.K., Smith, T.S., Fyhrrie, D.P. & Saad, M., 1999. Digital volume correlation: three-dimensional strain mapping using X-ray tomography, *Exp. Mech.*, **39**(3), 217–226.
- Bésuelle, P., 2001. Compacting and dilating shear bands in porous rock: theoretical and experimental conditions, *J. geophys. Res.*, **106**, 13 435–13 442.
- Bésuelle, P. & Rudnicki, J.W., 2004. Localization: shear bands and compaction bands, in *Mechanics of Fluid-Saturated Rocks*, pp. 219–321, eds Guéguen, Y. & Boutéca, M., Elsevier Academic Press.
- Bésuelle, P., Baud, P. & Wong, T.-f., 2003. Failure mode and spatial distribution of damage in Rothbach sandstone in the brittle-ductile transition, *Pure appl. Geophys.*, **160**, 851–868.
- Boutéca, M., Sarda, J.-P. & Schneider, F., 1996. Subsidence induced by the production of fluids, *Rev. Inst. Franc. Petrol.*, **51**, 349–379.
- Bruck, H.A., McNeill, S.R., Sutton, M.A. & Peters, W.H., 1989. Digital image correlation using Newton-Raphson method of partial differential correction, *Exp. Mech.*, **29**(3), 261–267.
- Casey, M. & Butler, R.W.H., 2004. Modelling approaches to understanding fold development: implications for hydrocarbon reservoirs, *Mar. Petrol. Geol.*, **21**, 933–946.
- Charalampidou, E.-M., Hall, S.A., Stanchits, S., Lewis, H. & Viggiani, G., 2011. Characterization of shear and compaction bands in a porous

- sandstone deformed under triaxial compression, *Tectonophysics*, **503**, 8–17.
- Charalampidou, E.-M., Hall, S.A., Stanchits, S., Viggiani, G. & Lewis, H., 2014. Shear-enhanced compaction band identification at the laboratory scale using acoustic and full-field methods, *Int. J. Rock Min. Sci.*, **67**, 240–252.
- Choquette, P.W. & Pray, L.C., 1970. Geologic nomenclature and classification of porosity in sedimentary carbonates, *AAPG Bull.*, **54**, 207–250.
- Churcher, P.L., French, P.R., Sham, J.C. & Schramm, L.L., 1991. Rock properties of Berea sandstone, Baker dolomite, and Indiana limestone, in *Proceedings of the SPE International Symposium on Oilfield Chemistry*, 1991 February 20–22, Anaheim, CA, Society of Petroleum Engineers, Richardson, TX, SPE 21044.
- Cilona, A., Baud, P., Tondi, E., Agosta, F., Vinciguerra, S., Rustichelli, A. & Spiers, C., 2012. Deformation bands in porous carbonate grainstones: field and laboratory observations, *J. Struct. Geol.*, **45**, 137–157.
- Cilona, A., Faulkner, D.R., Tondi, E., Agosta, F., Mancini, L., Rustichelli, A., Baud, P. & Vinciguerra, S., 2014. The effects of rock heterogeneity on compaction localization in porous carbonates, *J. Struct. Geol.*, **67**, 75–93.
- Dunham, R.J., 1962. Classification of carbonate rocks according to depositional texture, in *Classification of Carbonate Rocks*, pp. 108–121, ed. Ham, W.E., AAPG Memoir, 1.
- Eichhubl, P., Taylor, W.L., Pollard, D.D. & Aydin, A., 2004. Paleo-fluid flow and deformation in the Aztec sandstone at the Valley of Fire, Nevada—evidence for the coupling of hydrogeologic, diagenetic, and tectonic processes, *Geol. Soc. Am. Bull.*, **116**, 1120–1136.
- Eichhubl, P., Hooker, J.N. & Laubach, S.E., 2010. Pure and shear-enhanced compaction bands in Aztec sandstone, *J. Struct. Geol.*, **32**, 1873–1886.
- Fisher, Q.J., Casey, M., Clennell, M.B. & Knipe, R.J., 1999. Mechanical compaction of deeply buried sandstones of the North Sea, *Mar. Petrol. Geol.*, **16**, 605–618.
- Folk, R.L., 1980. *Petrology of Sedimentary Rocks*, Hemphill Publishing Company, 184 pp.
- Fredrich, J.T., Di Giovanni, A.A. & Noble, D.R., 2006. Predicting macroscopic transport properties using microscale image data, *J. geophys. Res.*, **111**, B03201, doi:10.1029/2005JB003774.
- Fredrich, J.T., Menéndez, B. & Wong, T.-F., 1995. Imaging the pore structure of geomaterials, *Science*, **268**, 276–279.
- Gleeson, J.W. & Woessner, D.E., 1991. Three-dimensional and flow-weighted NMR imaging of pore connectivity in a limestone, *Mag. Res. Imag.*, **9**(5), 879–884.
- Hall, S.A., 2006. A methodology for 7D warping and deformation monitoring using time-lapse seismic data, *Geophysics*, **71**(4), doi:10.1190/1.2212227.
- Hall, S.A., Lenoir, N., Viggiani, G., Desrues & Bésuelle, P., 2009. Strain localisation in sand under triaxial loading: characterisation by x-ray micro tomography and 3D digital image correlation, *Proceedings of the 1st Int. Symp. Comp. Geomech (ComGeo I)*, Juan-les-Pins, Cote d'Azur, France, 2009 April 29–May 1.
- Hall, S.A., Bornert, M., Desrues, J., Pannier, Y., Lenoir, N., Viggiani, G. & Bésuelle, P., 2010. Discrete and continuum analysis of localised deformation in sand using X-ray micro CT and volumetric digital image correlation, *Geotechnique*, **60**, 315–328.
- Ji, Y., Baud, P., Vajdova, V. & Wong, T.-f., 2012. Characterization of pore geometry of Indiana limestone in relation to mechanical compaction, *Oil Gas Sci. Tech. Rev. Inst. Fr. Pétr.*, **67**(5), 753–775.
- Kawakata, H., Cho, A., Kiyama, T., Yanagidani, T., Kusunose, K. & Shimada, H., 1999. Three dimensional observations of faulting process in Westerly granite under uniaxial and triaxial conditions by X-ray tomography scan, *Tectonophysics*, **313**, 293–305.
- Ketcham, R.A. & Carlson, W.D., 2001. Acquisition, optimization and interpretation of X-ray computed tomographic imagery: applications to the geosciences, *Comput. Geosci.*, **27**, 381–400.
- Kleinberg, R.L., 1999. Nuclear magnetic resonance, in *Experimental Methods in the Physical Sciences*, Vol. 35, pp. 337–385, eds Wong, P.-Z., Academic Press.
- Knackstedt, M.A., Latham, S., Madadi, M., Sheppard, A. & Varslot, T., 2009. Digital rock physics: 3D imaging of core material and correlations to acoustic and flow properties, *Leading Edge*, **28**(1), 28–33.
- Lenoir, N., Bornert, M., Desrues, J., Bésuelle, P. & Viggiani, G., 2007. Volumetric digital image correlation applied to X-ray micro tomography images from triaxial compression tests on argillaceous rock, *Strain*, **43**(3), 193–205.
- Lindquist, W.B., Venkatarangan, A., Dunsmuir, J. & Wong, T.-f., 2000. Pore and throat size distributions measured from synchrotron X-ray tomographic images of Fontainebleau sandstones, *J. geophys. Res.*, **105**, 21 509–21 527.
- Lorensen, W.E. & Cline, H.E., 1987. Marching cubes: a high resolution 3D surface construction algorithm, *Comp. Graph.*, **21**, 163–169.
- Louis, L., Wong, T.-f., Baud, P. & Tembe, S., 2006. Imaging strain localization by X-ray computed tomography: discrete compaction bands in Diemelstadt sandstone, *J. Struct. Geol.*, **28**, 762–775.
- Louis, L., Wong, T.-f. & Baud, P., 2007. Imaging strain localization by X-ray computed microtomography and digital image correlation: deformation bands in Rothbach sandstone, *J. Struct. Geol.*, **29**, 129–140.
- Lucia, F.J., 1995. Rock-fabric/petrophysical classification of carbonate pore space for reservoir characterization, *AAPG Bull.*, **79**, 1275–1300.
- Okabe, H. & Blunt, M.J., 2007. Pore space reconstruction of vuggy carbonates using microtomography and multiple-point statistics, *Water Res. Res.*, **43**, W12S02, doi:10.1029/2006WR005680.
- Otani, J., Mukunoki, T. & Sugawara, K., 2005. Evaluation of particle crushing in soils using X-ray CT data, *Soils Foundat.*, **45**, 99–108.
- Paterson, M.S. & Wong, T.-f., 2005. *Experimental Rock Deformation—The Brittle Field*, 2nd edn, Springer-Verlag.
- Pittman, E.D., 1971. Microporosity in carbonate rocks, *AAPG Bull.*, **55**, 1873–1878.
- Raynaud, S., Fabre, D., Mazerolle, F., Geraud, Y. & Latière, H.J., 1989. Analysis of the internal structure of rocks and characterization of mechanical deformation by a non-destructive method: X-ray tomodensitometry, *Tectonophysics*, **159**(1–2), 149–159.
- Rechenmacher, A.L. & Finno, R.J., 2004. Digital Image Correlation to evaluate shear banding in dilatative sand, *Geotech. Test J.*, **27**(1), doi:10.1520/GTJ11263J.
- Russell, S.S. & Sutton, M.A., 1989. Strain-field analysis acquired through correlation of X-ray radiographs of a fiber-reinforced composite laminate, *Exp. Mech.*, **29**(2), 237–240.
- Rustichelli, A., Tondi, E., Agosta, F., Cilona, A. & Giorgioni, M., 2012. Development and distribution of bed parallel compaction bands and pressure solution seams in carbonates (Bolognano Formation, Majella mountain, Italy), *J. Struct. Geol.*, **37**, 181–199.
- Sheldon, H.A., Barnicoat, A.C. & Ord, A., 2006. Numerical modelling of faulting and fluid flow in porous rocks: an approach based on critical state soil mechanics, *J. Struct. Geol.*, **28**, 1468–1482.
- Shipton, Z.K. & Cowie, P.A., 2001. Damage zone and slip-surface evolution over μm to km scales in high-porosity Navajo sandstone, Utah, *J. Struct. Geol.*, **23**, 1825–1844.
- Sun, W., Andrade, J.E., Rudnicki, J.W. & Eichhubl, P. 2011. Connecting microstructural attributes and permeability from 3D tomographic images of in situ shear-enhanced compaction bands using multiscale computations, *Geophys. Res. Lett.*, **38**, L10302, doi:10.1029/2011GL047683.
- Sutton, M., McNeill, S., Helm, J. & Chao, Y., 2000. Advances in two-dimensional and three-dimensional computer vision, in *Photomechanics*, pp. 323–372, ed. Rastogi, P.K., Springer.
- Tondi, E., Antonellini, M., Aydin, A., Marchegiani, L. & Cello, G., 2006. The role of deformation bands, stylolites and sheared stylolites in fault development in carbonate grainstones of Majella Mountain, Italy, *J. Struct. Geol.*, **28**, 376–391.
- Underwood, E.E., 1970. *Quantitative Stereology*, 274 pp., Addison Wesley.
- Vajdova, V., Baud, P., Wu, L. & Wong, T.-f., 2012. Micromechanics of inelastic compaction in two allochemical limestones, *J. Struct. Geol.*, **43**, 100–117.

- Wadell, H., 1935. Volume, shape and roundness of quartz particles, *J. Geol.*, **43**, 250–280.
- Wang, G., Zhao, S.Y. & Heuscher, D., 2002. A knowledge-based cone-beam x-ray CT algorithm for dynamic volumetric cardiac imaging, *Med. Phys.*, **29**(8), 1807–1822.
- Wattrisse, B., Chrysochoos, A., Muracciole, J.-M. & Néméz-Gaillard, M., 2001. Analysis of strain localization during tensile tests by digital image correlation, *Exp. Mech.*, **41**(1), 29–39.
- Wong, T.-f. & Baud, P., 2012. The brittle-ductile transition in rocks: a review, *J. Struct. Geol.*, **44**, 25–53.
- Zhan, X., Schwartz, L.M., Toksoz, M.N., Smith, W.C. & Morgan, F.D., 2010. Pore-scale modeling of electrical and fluid transport in Berea sandstone, *Geophysics*, **75**, F135–F142.
- Zhu, W., Baud, P. & Wong, T.-f., 2010. Micromechanics of cataclastic pore collapse in limestone, *J. geophys. Res.*, **115**, B04405, doi:10.1029/2009JB006610.